

## **Piezoelectric fibers for sensing and actuation at ultrasonic and audio frequencies**

### **Project Staff**

Zheng Wang, Noémie Chocat, Shunji Egusa, Zach M. Ruff, A. M. Stolyarov, Dana Shemuly, Fabien Sorin, John D. Joannopoulos, Yoel Fink

### **Sponsors**

ISN/ARO, DARPA, NSF

Following the first demonstration of fiber-based piezoelectric element that can be interfaced with external circuits in both transmitter and receiver configurations, we continue to explore the refinement of the fabrication process on novel and high performance structures: fibers with circular and rectangular cross sections have been fabricated to control the acoustic wavefronts. Fibers containing piezoelectric stacks are developed to allow increased signal to noise ratio for both acoustic emission and acoustic reception. Electrical impedance measurements have been employed to characterize and understand the piezoelectric (ferroelectric) properties of both the fiber transducer and its active component materials.

In fabricating high-performance piezoelectric fibers, significant challenges and seemingly conflicting requirements must be resolved. The necessity to utilize crystalline materials both for the piezoelectric layer and the electrical conductors leads to the formation of multiple adjacent low viscosity and high aspect ratio domains. These domains undergoing a reduction in cross sectional dimensions are susceptible to capillary breakup and mixing during fiber drawing due to flow instabilities. Layer thickness non-uniformity either in the lateral or in the longitudinal directions precludes the formation of the coercive field needed for poling. Moreover, even if capillary breakup were kinetically averted and uniform sections of fibers were to emerge they would not exhibit piezoelectricity because the stress and strain conditions necessary to induce the thermodynamic phase transition in PVDF cannot be sustained in the fiber draw process.

To address these challenges we choose to focus our attention on the ability to maintain geometric coherence and layer thickness uniformity. A viscous and conductive carbon-loaded poly(carbonate) (CPC) is used to confine the low viscosity crystalline piezoelectric layer during the draw process. The CPC layers exhibit high viscosity (105~106 Pa-s) at the draw temperature and adequate conductivity (103~106 ohm/cm) over the frequency range from DC to tens of MHz, thus facilitating short range (hundreds of microns) charge transport on length scales associated with the fiber cross section. Then a piezoelectric polymer which crystallizes into the appropriate phase is identified. Poly(vinylidene-fluoride-Trifluoroethylene) copolymer (P(VDF-TrFE)) assumes the ferroelectric  $\beta$  phase spontaneously upon solidification from the melt without necessitating any mechanical stress, making it particularly suitable for the thermal fiber drawing process.

The fiber draw is realized in a stress and temperature regime dominated by viscous forces (as opposed to surface tension) allowing for non-equilibrium geometries (Figs.1a, 1b) to be realized this in turn allows one in-principle to tailor the acoustic wavefronts and the radiation patterns dictated by the fiber geometry. A circular geometry, typical in conventional fiber constructs, emits acoustic waves omnidirectionally. In contrast, at frequencies where the acoustic wavelength is comparable to the dimension of the fiber cross sections, flat fiber surfaces produce highly directional acoustic emissions, while the emission is suppressed near the narrow apexes as shown in finite element calculations depicted in Figure 1c.

The potential to modulate sophisticated optical devices in a single-fiber structure is continued to be explored (Figure 1b). Piezoelectric fibers with an integrated Fabry-Perot (FP) optical cavity can control its resonant frequency through electrical modulation directly applied to the embedded piezoelectric element. These piezoelectric FP fibers are mechanically robust and yet flexible; and can be assembled into a fabric for large area coverage as shown in Figure 1d. The manifested

color of the fabric is the reflection from the third order band of the Fabry-Perot optical structure embedded in the fibers.

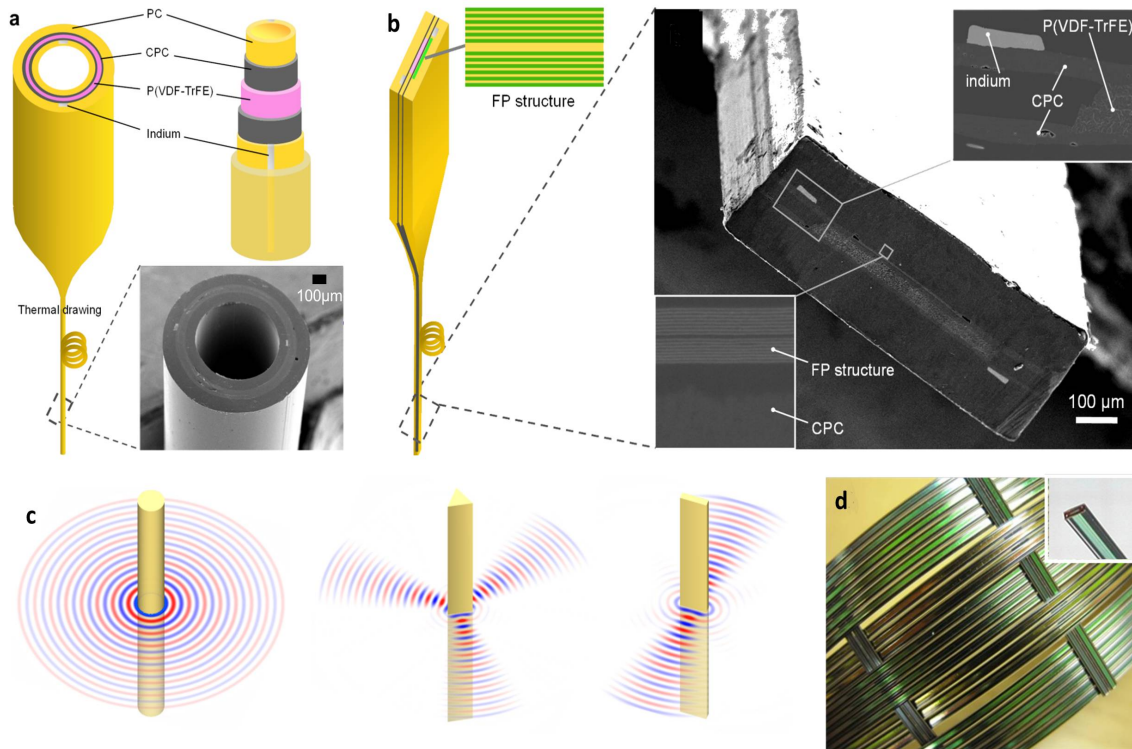


**Figure 1.** Structure of geometrically-shaped piezoelectric fibers. a, Schematic of the fabrication process of a cylindrical piezoelectric fiber. A preform is constructed by consolidating a shell of P(VDF-TrFE), shells containing CPC/indium electrodes, and PC cladding. A SEM micrograph of the cross section of a cylindrical piezoelectric fiber is shown in the inset. b, Schematic of the fabrication process of an integrated piezoelectric FP rectangular fiber. A FP optical cavity is embedded with the piezoelectric structure in a preform. The preform is thermally drawn into a micro-structured fiber. A SEM micrograph of the cross section of an integrated piezoelectric FP fiber is shown on the right. c, Near-field pressure patterns of the acoustic emission at 1.3MHz from a circular fiber, a triangular fiber and a rectangular fiber with cross-sectional dimensions around 2mm. d, Two-dimensional device fabric constructed by knitting the piezoelectric/FP fibers as threads. Inset is a photograph of an individual fiber.

The mechanical strain needed for piezoelectric modulation of integrated optical resonance demand electric fields approaching the poling voltage for single-layer P(VDF-TrFE) elements on the order of a few kV. Common electrical interface at audible and ultrasound frequencies typically operates at a voltage level of several volts. Due to this practical constraint, it is therefore important to achieve large mechanical displacement using stacked multilayer structures. We have identified a conductive polymer material, carbon-doped polyethylene, which can be folded into layered electrode stacks while maintaining its electrical conductivity and connectivity. Excellent uniformity has been observed across the multilayer stack (Figure 2). Such fibers containing a piezoelectric stack have shown pronounced audible response upon poling, in comparison to single-layer fiber samples.

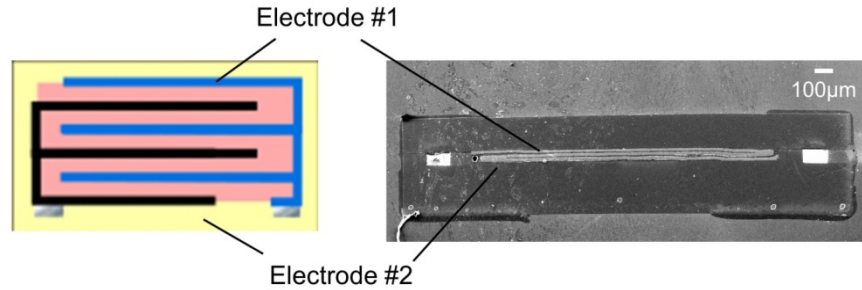


**Figure 2.** Schematic of a piezoelectric fiber containing a folded transducer stack. Both electrodes consist of thin films of carbon-doped polyethylene films and are in contact with metal wire for high conductivity along the longitudinal direction. A SEM micrograph of a fabricated 3-fold fiber is shown on the right.

We have performed direct acoustic measurements, using the fibers both as an acoustic sensor and as an acoustic actuator centred at 1 MHz. Such a frequency range is typical in ultrasound imaging applications. A water-immersion ultrasonic transducer (Olympus Panametrics-NDT, 1.0 MHz-centered) is coupled to a fiber sample across a water tank to match the acoustic impedance. The fiber sample is attached to the water tank surface via immersion gel, with the piezoelectric layer facing towards the transducer. The rectangular geometry further improves the acoustic directionality. At MHz frequencies, capacitive electromagnetic coupling between the transducer circuit and the receiver charge amplifier can be significant even with careful shielding and grounding. To separate the acoustic signals from the electromagnetic interference, we use a pulsed excitation and time-gate the received signals, exploiting the 5 orders of magnitude difference in the propagation speed between acoustic and electromagnetic pulses.

Frequency domain characterizations of the flat rectangular piezoelectric fibers are performed with a fixed transducer-to-fiber distance, with the pulsed excitation and the time-gated signal processing (Figure 3a). The measured piezoelectric response of the fiber, both as a sensor and an actuator, essentially follows the intrinsic frequency profile of the transducer. Here the frequency range is limited here by the bandwidth of the transducer, corroborated with the impedance measurement (Figure 3b). The conductivity of the polymer electrodes imposes an upper limit on the operational frequency, above which the RC delay exceeds the time to fully charge and discharge the entire piezoelectric capacitor. The axial conductivity is guaranteed by the metal wires in contact with the polymer electrodes. Since polymeric piezoelectric materials are in principle broadband, the piezoelectric fibers could operate at a far broader range of frequencies, with the use of polymer electrodes with higher conductivity. Nevertheless, the fabricated fiber samples function over both ultrasonic and audible frequencies. For example, similar fibers were used to generate audible sound between 7 kHz and 15 kHz with a driving voltage of 5V.

Monolithic processing of piezoelectric transducers in fibre form presents opportunities in a variety of applications that are well matched to the fibre's geometry. For example fabrics woven from piezoelectric fibres could be used as a communication transceiver. With a high sensitivity to stress and pressure, such fabrics may be used in bullet-proofing vests to monitor the impact dose over a large area of the torso. Nylon fabrics containing piezoelectric fibers can produce electric signals in response to external strain, which could find important applications in parachute research and self-monitoring. Finally, uniform piezoelectric fibres have been prepared in tens of metres, ideal for distributed sensing: their sensitivity to stress and strain combined with their low profile make them ideal for constructing minimally-perturbative (sparse) sensor meshes for studying large-area distributions of the pressure and velocity fields in myriads of fluid flow applications including oceanic current monitoring. In addition, the capability of fabricating acoustic fibres with arbitrary cross-sections allows for integrating additional ferroelectric functionalities in a single-fibre device, such as energy conversion and other actively modulated devices.

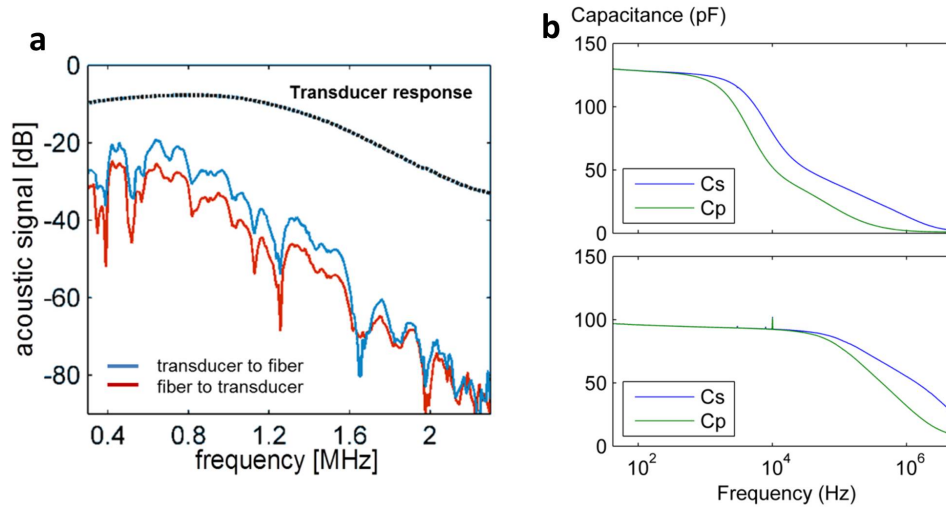


**Figure 3.** a. Acoustic signal detected (blue curve) and emitted (red curve) by a piezoelectric rectangular fiber around 1 MHz. The dotted line is the power spectrum of the (1 MHz-centred) transducer used. b. Frequency-dependent capacitance of the piezoelectric rectangular fiber. A fiber without embedded metal wires (the upper panel) shows a cut-off frequency around 10kHz, characterized by the reduction of measured capacitance. A fiber that is axially conductive through metal wires (the lower panel) shows a bandwidth up to 1MHz.

## Ovonic Memory Switching in Multimaterial Fibers

### Academic and research staff

Sylvain Danto, Zachary M. Ruff, Zheng Wang, John D. Joannopoulos, Yoel Fink

### Sponsor

DARPA, ISN, DOE, NSF

Here we report on the capability of ovonic memory switching inside thermally-drawn composite fiber devices. Key to this breakthrough is the incorporation of high Te-content amorphous semiconductors in contact with metallic electrodes inside fibers. It makes possible to electrically and reversibly modulate *in-situ* the electronic structure of the semiconductor between a high-resistance amorphous (OFF) state and a low-resistance crystalline (ON) state. In the emerging field of flexible electronic, the principle of phase-change switching inside a fiber offers a potential for large coverage-area, light-weight and low cost devices with unusual functionalities.

Ovonic memory switching is widely used in modern data storage media [1]. It is based on the property of phase-change materials (PCMs) to cycle under electrical impulsions between a high-R amorphous (OFF) state and a low-R crystalline (ON) state while producing a large electrical contrast for unambiguous reading [1]. At a critical threshold voltage ( $V_{th}$ ), PCMs spontaneously generate electronic filaments which triggers by Joule self-heating the formation of a crystalline phase, stabilizing the material into a permanent low-R state (SET operation). The ON-to-OFF transition (RESET operation) is caused by the application of a higher current pulse. The ON/OFF transitions yield orders-of-magnitude changes in the electrical resistance. The development of PCMs for memory media has proceeded from Te-based amorphous semiconductors, more specifically from the eutectic  $\text{Ge}_{17}\text{Te}_{83}$  alloy doped with elements such as Sb.

Recently, we have developed a metal-semiconductor-polymer fiber processing approach [2-6]. It allows the production of nanometer features extending over the meter-long axis of the device with unique functionalities. This technique imposes however the use of thermally stable glass. On the other hand, memory switching necessitates highly versatile materials. In order to reconcile these requirements, we selected the  $\text{Ga}_{10}\text{Ge}_{15}\text{Te}_{75}$  (GGT) and  $\text{Ge}_{22}\text{As}_{18}\text{Se}_{15}\text{Te}_{45}$  (GAST) glasses. On one hand, they both exhibit the required viscosity-temperature dependence to support the draw tension. On one other hand, being chemically close to the  $\text{Ge}_{17}\text{Te}_{83}$  alloy, they exhibit favorable characteristics in terms of switching property: high tendency for crystallization, high electrical conductivity with a strong temperature dependence electrical conductivity.

We first proceed to demonstrate switching inside composite fiber and the temperature dependence of the threshold voltage (Figure 1). We use a GGT fiber made of a solid GGT core contacted by two ZnSn electrodes ( $T_m = 199\text{ }^\circ\text{C}$ ) and surrounded by a polysulfone (PSU) cladding ( $T_g = 165\text{ }^\circ\text{C}$ ) and a GAST fiber, the later one consisting of a solid GAST core contacted by four Sn electrodes ( $T_m = 232\text{ }^\circ\text{C}$ ) and surrounded by a polyethersulfone (PES) cladding ( $T_g = 225\text{ }^\circ\text{C}$ ) (Figure 1a). Both devices exhibit a clear switching behavior, which follows a similar pattern (Figure 1b). As the bias gradually increases, the current quickly evolves from an ohmic to a non-linear behavior. At the critical voltage  $V_{th}$ , the OFF-to-ON transition takes place; the current overshoots to a very high value and the sample switches to a stable low-R state. The exponential temperature dependence of  $V_{th}$  satisfies the Arrhenius relation:  $V_{th}(T) = V_0 \exp[\Delta\varepsilon/k_B T]$  where  $\Delta\varepsilon$  is the threshold voltage activation energy,  $V_0$  a constant,  $k_B$  the Boltzmann constant and  $T$  the absolute temperature (Figure 1c). From the slope of the curves we calculate  $\Delta\varepsilon_{GGT} = 0.18\text{ eV}$  and  $\Delta\varepsilon_{GAST} = 0.29\text{ eV}$ .

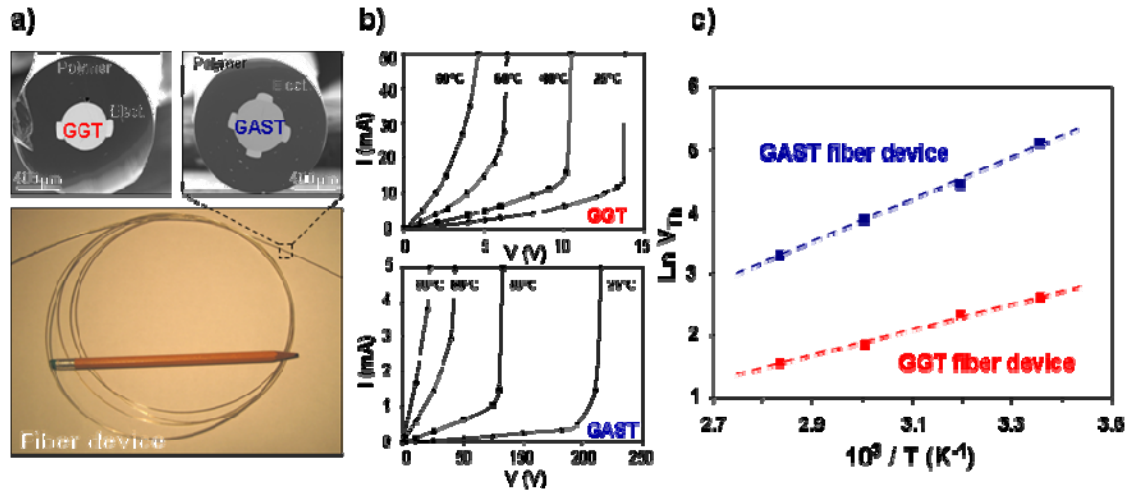


**Figure 1.** Phase-change memory switching in fibers (a) Photographs of a typical memory fiber (bottom panel). SEM micrographs of the cross-section of a GGT fiber (top left) and a GAST fiber (top right). (b)  $I$ - $V$  characteristics of a GGT fiber (top) and a GAST fiber device (bottom) at various temperatures ( $I_{fiber} = 12$  cm). (c) For both fibers, the threshold voltage as a function of the temperature agrees well with Arrhenius relations (dashed lines).

The most remarkable property of the resistive switching materials is their ability to cycle under applied bias between the OFF and ON states. Here we reproduce this effect in fibers. We make use for this study of a 12-cm-long GAST fiber. The  $I$ - $V$  characteristic SET / RESET cycle follows the schematic pattern described in Figure 2a. The SET operation consists in raising the voltage above the threshold value. The SET current pulse yields a local raise in the temperature of the glass and ultimately its crystallization. Reversibly, the RESET operation consists in increasing the current even further. The  $I_{RESET}$  pulse locally melts the previously written low-R channel which, by contact with the surrounding material, quenches back into the glassy state. We subject the device to a complete SET / RESET cycle for two different SET current limitations:  $I_{SET} = 2.5$  mA and 11.5 mA (Figure 2b). In the case  $I_{SET} = 2.5$  mA, the resistance drops by  $\sim 3$  orders-of-magnitude (so-called “low-ON state”) and  $I_{RESET} \sim 4$  mA. In the case  $I_{SET} = 11.5$  mA, the resistance fluctuates by  $\sim 4$  orders-of-magnitude (so-called “High-ON state”) and we have  $I_{RESET} \sim 20$  mA. As  $I_{SET}$  increases from 2.5 to 11.5 mA, the cross-section and thermal stability of the crystalline filament increases. By consequence, the RESET current increases concomitantly with  $I_{SET}$ , from  $I_{RESET} = 4$  mA to 20 mA.

The electrically-driven *in-situ* phase-change switching inside a fiber hold promises for the integration of complex electronic functionalities into flexible and light-weight devices. It bridges two traditional yet, to date, mutually exclusive domains of applications of the amorphous semiconductors: data storage and fiber optic technologies. Using the *in-situ* phase-change technique, we envision implementing multiple independent electronic components along the fiber stretched out axis. One other potential application consists in the design of cross-bar fabric-array devices.

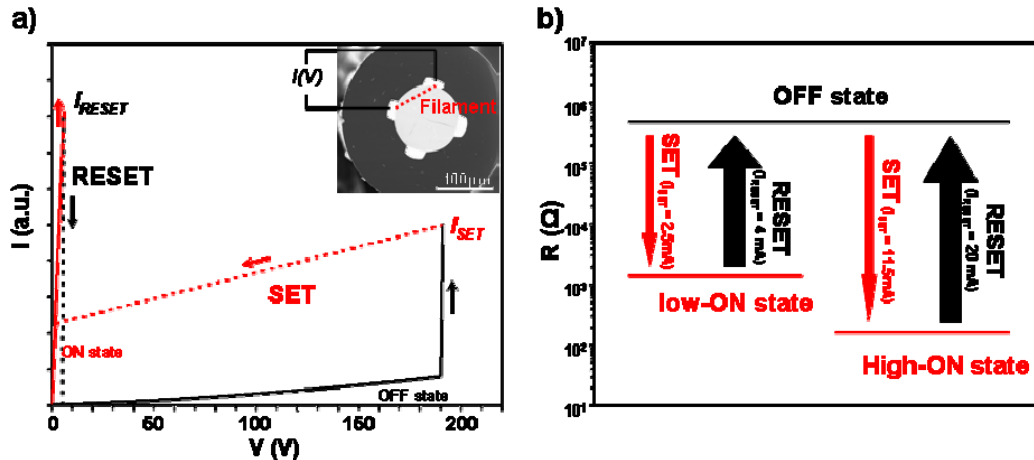


Figure 2. Reversible switching in GAST phase-change memory fiber ( $I_{\text{fiber}} = 12 \text{ cm}$ ).

(a) The evolution of the current-voltage characteristics in a SET / RESET operation (inset: SEM cross-section GAST fiber. The low-R crystalline path solely links the two electrically connected electrodes) (b) ON / OFF resistance cycling of the device for two different SET current limitations ( $I_{\text{SET}} = 2.5 \text{ mA}$ : low-ON state,  $I_{\text{SET}} = 11.5 \text{ mA}$ : high-ON state).

#### References:

- [1] M. Wuttig, N. Yamada, *Nat. Mat.* **2007**, 6, 824.
- [2] A. F. Abouraddy, M. Bayindir, G. Benoit, S. D. Hart, K. Kuriki, N. Orf, O. Shapira, F. Sorin, B. Temelkuran, Y. Fink, *Nat. Mat.* **2007**, 6, 336.
- [3] F. Sorin, O. Shapira, A. F. Abouraddy, M. Spencer, N. D. Orf, J. D. Joannopoulos, Y. Fink, *Nano Lett.* **2009**, 9, 2630.
- [4] D. S. Deng, N. D. Orf, S. Danto, A. F. Abouraddy, Y. Fink, J. D. Joannopoulos, *Appl. Phys. Lett.* **2010**, 96, 023102.
- [5] S. Danto, F. Sorin, N.D. Orf, Z. Weng, S.A. Speakman, J.D. Joannopoulos, Y. Fink, *Adv. Mat.* **2010** (in press).
- [6] S. Egusa, Z. Wang, N. Chocat, Z. M. Ruff, A. M. Stolyarov, D. Shemuly, F. Sorin, P. T. Rakich, J. D. Joannopoulos, Y. Fink, *Nat. Mat.* **2010** (in press).

## Enabling coherent superpositions of iso-frequency optical states in multimode fibers

### Project Staff

Ofer Shapira, Ayman F. Abouraddy, Qichao Hu, Dana Shemuly, John D. Joannopoulos, and Yoel Fink

### Sponsors

DARPA, ISN, NSF

The ability to precisely and selectively excite superpositions of specific fiber eigenmodes allows one in principle to control the three dimensional field distribution along the length of a fiber. Here we demonstrate the dynamic synthesis and controlled transmission of vectorial eigenstates in a hollow core cylindrical photonic bandgap fiber, including a coherent superposition of two different angular momentum states [1]. The results are verified using a modal decomposition algorithm that yields the unique complex superposition coefficients of the eigenstate space.

Waveguides supporting a multiplicity of iso-frequency states are characterized by an entropic increase in the population of states due to axially distributed perturbations. Initiating and maintaining a specific population through a controlled excitation and transmission of coherent superposition of eigenstates in a “constant entropy” regime can be highly desirable. The motivation is twofold. First, the formation of three dimensional field distributions can be achieved along the longitudinal dimension of a fiber providing a new medium for controlled light matter interactions. Second, the larger modal area and the controlled excitation could enable high-power lasers and waveguides to operate in higher energies without compromising the beam quality. Here we introduce an approach to synthesize, controllably transmit, and analyze coherent superpositions of fiber eigenmodes beyond the traditional single mode excitation. We show that in fact one may produce coherent linear superpositions of iso-frequency vectorial modes with different angular momenta and control their weights in real time.

In the past, coupling preferentially to a single specific fiber mode of weakly multimoded fibers has been achieved through the introduction of perturbations to the fiber structure such as fiber bends [2], gratings [3], or radial modulation to the refractive index profile [4]. Other approaches involve the modulation of the input beam phase or amplitude either by the fabrication of subwavelength polarization masks [5], or using a spatial light modulator (SLM) [6,7]. Nevertheless, to date, the controlled excitation and transmission of a coherent superposition of eigenstates has yet to be demonstrated. Indeed very little work has been done on the active use of controlled excitation of many-mode systems, predominantly due to the difficulty in synthesizing the required multi-mode profile, controlling its transmission, and the lack of a reliable approach to confirm the content of the propagated beam.

To demonstrate this approach, a cylindrically symmetric hollow-core photonic band gap fiber with core diameter of 68  $\mu\text{m}$  was drawn using the preform-based fabrication method [8-10]. Such fiber supports several thousands of vectorial leaky-modes by confining light in the hollow core region via omnidirectional reflection from the cylindrically symmetric multilayer structure lining the core [11,12]. The electric field of the  $n$ th mode of such structure is given by  $\Psi_n(\mathbf{r}) \exp(-i\omega t) = \mathbf{R}_n(r) \exp[i(\beta_n z - \omega t + m\theta)]$  with three conserved quantities: the frequency  $\omega$ , the axial wave vector  $\beta_n$ , and the angular momentum  $m$ . The total electric field can then be expressed by  $\Psi(\mathbf{r}) = \sum_n c_n \Psi_n(\mathbf{r})$  where  $c_n$  are the complex expansion coefficients. In particular we study the superposition of two of the fundamental modes of this fiber by sculpting the phase profile of a Gaussian laser beam using a SLM and introducing it into the hollow-core fiber. Our choice of direct phase modulation, as opposed to holographic techniques, stems from the desire to avoid the computational latency associated with hologram calculations, allowing real time dynamic manipulation of the field. We verify that the desired superposition is achieved by using a modal

decomposition technique that yields the complex expansion coefficients of the core-confined modes from intensity images of the fiber output [13]. The results of the modal decomposition confirm that we are in fact smoothly varying the relative weights of the two selected modes in a controlled manner. Note that, this technique is quite general and may be used in optical waveguides other than fibers and in any spectral range.

A common difficulty when dealing with many-mode waveguides is the inadvertent mode coupling that occurs along the fiber length due to perturbations to the fiber structure. While the exact coupling strength between two modes depends on the nature of the perturbation, in many practical cases, to a good approximation [11], the power that couples from one mode  $\Psi_n$  to another  $\Psi_{n'}$  is proportional to  $\Delta\beta_{nn'}^{-2}$  where  $\Delta\beta_{nn'} = \beta_{n'} - \beta_n$  is the mode separation. From general phase-space arguments it can be shown that the mode separation scales as  $\Delta\beta \sim R^{-2}$  with  $R$  being the core radius. Using these general scaling arguments, the mode coupling strength due to intentional perturbations such as fiber bends can be induced or inhibited by controlling the fiber bend radius. In the PBG fiber used here, with core diameter of roughly 45 wavelengths the fiber bend radius should be kept above 46 cm in order to inhibit any significant mode coupling. Mode coupling can also occur due to unintentional perturbations such as mechanical stress, microbends, or manufacturing imperfection. In such cases the strategy is to weaken the coupling strength by reducing the core diameter while assuring the fiber still supports the modes of interest.

For definiteness, we focus on two selected modes of this fiber, the  $TE_{01}$  and the  $HE_{11}$ . The intensity profile and polarization of the modes are shown in Figure a. The  $TE_{01}$  with angular momentum zero is non-degenerate, purely transverse, with polarization vortex at the origin and doughnut shaped intensity profile. The  $HE_{11}$  is the lowest energy, double degenerate, hybrid mode with Gaussian like beam profile. We note that the  $TE_{01}$ , the lowest-loss mode for such a fiber structure, is linearly polarized in  $\hat{e}_\theta$ , and has complete angular symmetry. Thus, unlike the usual doubly degenerate linearly polarized modes of a “single-mode” fiber, such a mode is truly single mode, and would thus avoid the usual pitfall of polarization mode dispersion [14]. The  $HE_{11}$  mode is linearly polarized (in Cartesian coordinates) and has angular momentum one. The transmission bandwidth of the  $HE_{11}$  is expected to be strongly affected by the narrower transverse magnetic (TM) band gap.

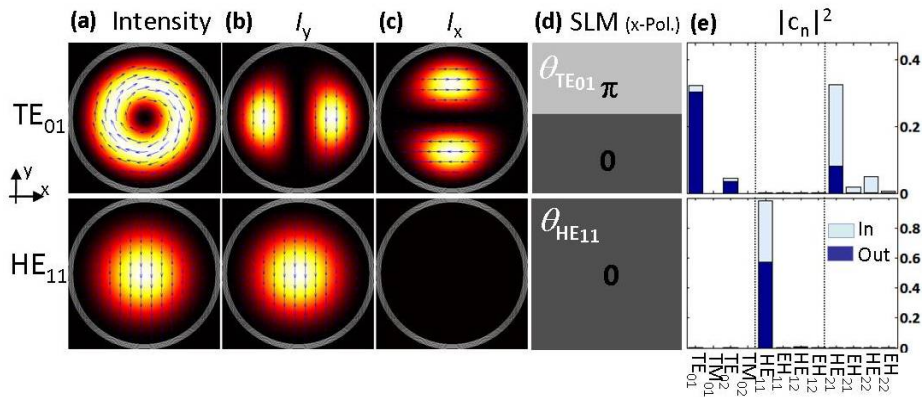


**Figure 1** (color). (a) Calculated intensity distributions of the  $TE_{01}$  (upper panel) and  $HE_{11}$  (lower panel) modes alongside their  $\hat{y}$  (b) and  $\hat{x}$  (c) polarizations. The SLM phase distributions (d) that are imparted to the  $\hat{x}$ -polarized Gaussian laser beam and the corresponding calculated coupling (e) to the twelve lowest modes with  $m < 3$  at the input (light blue) and after propagation through a meter long fiber (dark blue) taking into account differential modal losses.

One characteristic of these modes that is of importance in the discussion that follows is that each polarization component of the  $HE_{11}$  field has a constant phase, while the  $TE_{01}$  field has two halves that differ by  $\pi$ , parallel to the polarization of the linear projection (Figure b-c). Since in general,

modes supported by this fiber are vectorial, two orthogonal polarization components of the field need to be modulated in order to synthesize a perfect eigenstate. However, we note that modulation of a single polarization component using single SLM can result in preferential excitation owing to the differential modal losses of the PBG fiber [11]. The strategy to excite such low-energy modes can be therefore to modulate the phase distribution of the incident beam with the phase of one polarization component of the desired mode. The two phase distributions presented in Figure d when imparted to a Gaussian beam profile result in nearly single mode propagation after a meter long fiber. Figure e provides theoretical calculation of the coupling coefficients at the input facet for each phase pattern (light blue) and at the output facet (dark blue) taking into account the propagation loss of each mode. Thus, the simple control over the phase front, together with the fiber inherent mode filtering, suggests that one not only may controllably switch between these different modes but can also controllably excite superpositions of these modes.

We used a linearly polarized laser beam at  $1.5 \mu\text{m}$  from a tunable optical parametric oscillator (MIRA OPO, Coherent) that is synchronously pumped with a Ti:Sa laser (MIRA, Coherent) as our source. Figure a depicts the optical setup in which the linearly polarized Gaussian beam from our source is spatially filtered and magnified before it impinges normally on a reflective SLM (SLM PPM x7550, Hamamatsu) through a beam splitter. Then it reflects back to a lens (focal length 15 cm) that couples the beam to the fiber. The SLM imparts a computer-controlled phase distribution to the optical wave front. The beam at the output of the fiber is imaged using a microscope objective (x40) onto an InGaAs CCD camera (NIR SU320-1.7RT, Sensors Unlimited, Inc.).

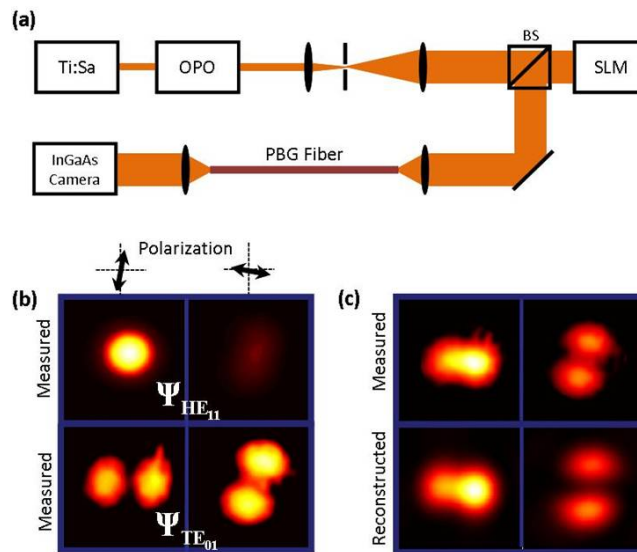


**Figure 2** (a) Schematic of the optical setup. (b) Measured intensity distribution for two perpendicular polarizations of the  $HE_{11}$  (upper panel) and  $TE_{01}$  (lower panel). (c) Far-field intensity patterns of the measured (upper panel) and reconstructed (lower panel) superposition of the two modes for  $a=0.625$ .

Applying the constant phase distribution,  $\theta_{HE_{11}}$ , to the SLM results in strong coupling to the  $HE_{11}$  mode as apparent from the measured near-field intensity images (upper panel of Figure b) taken at two perpendicular polarizations by placing linear polarizer between the exit of the fiber and the camera. To preferentially excite the  $TE_{01}$  mode,  $\theta_{TE_{01}}$  is imparted to the beam. This overlaps with one Cartesian polarization of the  $TE_{01}$  and thus couples to it with maximum efficiency of 37% but also with the same efficiency to the  $HE_{21}$  (upper panel of Figure e). However since the propagation length of the  $HE_{21}$  is shorter than of the  $TE_{01}$ , as indicated by Figure e, the measured intensities after a meter long fiber indicates predominant  $TE_{01}$  component at the fiber output. Exact analysis of those measurements using mode decomposition technique is presented at the next section. 8. All measurements were performed at  $1.5 \mu\text{m}$  wavelength, lying inside the fiber

transmission photonic band gap. It is interesting to note that tuning the wavelength of the input field outside the TM band gap while staying inside the broader TE band gap results solely in the excitation of an extremely pure  $TE_{01}$  mode regardless of the input coupling condition. This can be understood by the fact that even small residual coupling to TE mode survives the propagation through the fiber while other modes are not guided at all.

While it may be possible to identify some of the simpler low-order modes by using a linear polarizer to obtain intensity projection profiles, the same is not possible when the beam is a superposition of such modes. In such cases a distinct approach is required that reliably decomposes the output beam into its constituent modes revealing the relative (complex) contribution of each eigenmode,  $c_n$ . We previously developed a non-interferometric approach to achieve modal decomposition of the fields at the output of a general waveguide [13]. The technique utilizes a mapping of the two-dimensional field distribution onto the one-dimensional space of waveguide eigenmodes, together with a phase-retrieval algorithm to extract the amplitudes and phases of all the guided vectorial modes. This approach necessitates the acquisition of two near-field and two far-field intensity measurements at orthogonal polarizations. Here, near-field measurements were obtained by imaging the fiber facet to the camera using the microscope objective lens, while the far-field measurements were obtained by recording the output of the fiber with no lens. The size of the fiber core ensures that the diffracted field after a free-space propagation of one centimeter already corresponds to the far field.

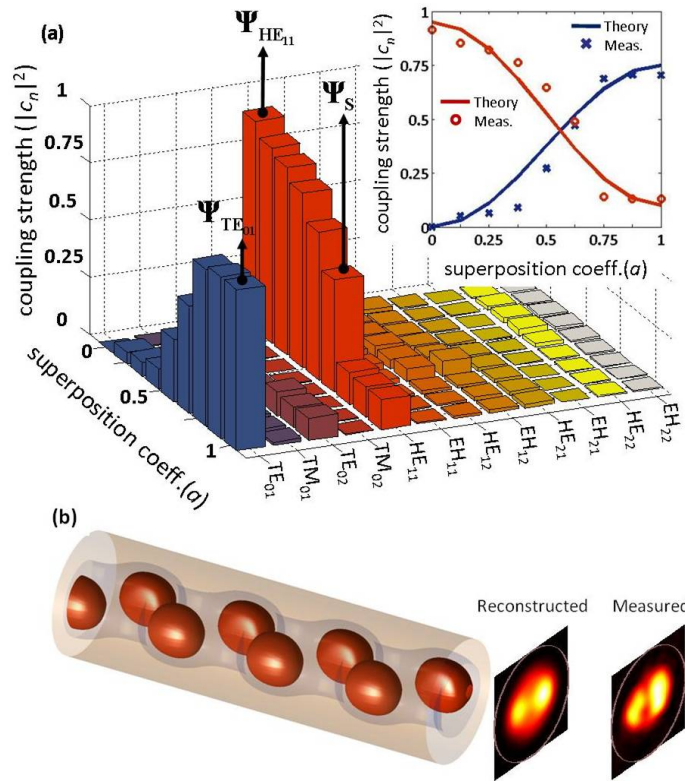


**Figure 3** (a) Coupling strength of the different modes as obtained from the mode decomposition algorithm for several values of the superposition coefficient  $a$ . The inset shows consolidated results for the main two modes together with theoretical calculation of the expected coupling coefficients. (b) Three-dimensional time averaged intensity pattern of the superposition defined by  $a=0.625$  presented over 3.75 beat lengths ( $2\pi\Delta\beta^{-1}$ ) of the two modes. To the right, the reconstructed and measured intensities at the end facet of the fiber are compared.

We have shown above that switching the phase distribution imparted to the beam from  $\theta_{HE_{11}}$  to  $\theta_{TE_{01}}$  results in the output beam switching between the  $HE_{11}$  and  $TE_{01}$  modes. It is thus reasonable to expect that a weighted sum of the two phases will result in a beam which is composed of a weighted superposition of the two modes. More explicitly, in the limit where the two modes dominate the population of the output beam, by setting the SLM with the superposition phase  $\theta_s = a \cdot \theta_{TE_{01}} + (1-a) \cdot \theta_{HE_{11}}$  where  $a$  is the superposition coefficient, the relative weight of the  $TE_{01}$  mode is expected to be  $c_{TE_{01}} = c_0 \exp[i\pi(1-a)/2] \cos[\pi(1-a)/2]$  where  $c_0$  is the relative weight that corresponds to  $\theta_{TE_{01}}$  ( $a=1$ ). We have implemented the above outlined idea experimentally by varying the phase of one half of the phase image from 0 to  $\pi$  while keeping the other half fixed to 0, corresponding to varying  $a$  from 0 to 1. For each value of  $a$  we acquired the four required intensity images. We applied the mode decomposition algorithm for each set and obtained the complex coefficients of the first 12 lowest energy modes with  $m < 3$ . Examples of the acquired far-field intensity images for  $a=0.625$  are shown in Figure c together with the intensity images of the reconstructed field. Neglecting modes with  $|c_n|^2 < 0.1$ , the coherent superposition as obtained from the mode decomposition algorithm is  $\Psi_S = 0.69 e^{i0.64} \Psi_{TE_{01}} + 0.7 \Psi_{HE_{11}}$ . The absolute square of the coefficients for each value of  $a$  for all considered modes are shown graphically in Figure a. As expected, the weight of the  $HE_{11}$  is maximal for  $a=0$ , and that of the  $TE_{01}$  is maximal for  $a=1$ . For intermediate values a controlled superposition of the two eigenstates is obtained. The inset of Figure a shows the relative weight of the  $TE_{01}$  and  $HE_{11}$  modes with the expected theoretical line obtained from the expression for  $c_{TE_{01}}$ . The small discrepancies between the measurement and the theoretical values are attributed to the weak excitation of other modes that are neglected by the approximation made to the expression of  $c_{TE_{01}}$ . The weak population of other modes at the output of the fiber is attributed to fast-decaying modes that are excited either by the input beam (as suggested by Figure e) or inadvertently due to system imperfections. In the previously discussed case of  $a=1$  the relative weights of the measured modes as obtained from the decomposition (Figure a) and the theoretical values (Figure e) closely match for the  $TE_{01}$  and the  $TE_{02}$ , 0.72 and 0.1 respectively, while some discrepancies are observed for the  $HE_{11}$  and  $HE_{21}$ . The differences are attributed to possible misalignment of the input beam with respect to the fiber's core which can give rise to inadvertent excitation of modes as well as differential losses due to surface roughness at the core boundary interface.

This ability to control the eigenstates population provides a mean to determine and tailor the three dimensional field distribution along the fiber axis. Figure b shows the time averaged intensity distribution of  $|\Psi_S|^2$  calculated for a longitudinal distance of several  $\Delta\beta^{-1}$  until the end facet of the fiber where the measured and calculated cross section patterns are presented and compared. This result demonstrates the ability to construct a volumetric intensity (and field) patterns inside the fiber from knowledge of the complex expansion coefficients through control excitation of eigenstates at the input and verification of the modal content at the output of a waveguide. While this intriguing result is obtained by populating only two eigenstates in the superposition, scaling up to many modes can be achieved by the modulation of both polarization states. Since a single SLM allows the modulation of only one polarization component, the modal distributions that may be excited in the eigenstate space is limited to those that include modes with slower decay lengths than the superfluous modes that are excited due to the imperfect field structure at the input to the fiber. A complete control could be achieved by modulating both the phase and amplitude of the vectorial field by using an additional SLM or dividing the SLM pixel array to two regions treating each polarization separately.

## References

1. Ofer Shapira, Ayman F. Abouraddy, Qichao Hu, Dana Shemuly, John D. Joannopoulos, and Yoel Fink, "Enabling coherent superpositions of iso-frequency optical states in multimode fibers", *Opt. Express* **18**, 12622 (2010).
2. M. Skorobogatiy, C. Anastassiou, S. G. Johnson, O. Weisberg, T.D. Engeness, S.A. Jacobs, R.U. Ahmad, and Y. Fink, "Quantitative characterization of higher-order mode converters in weakly multimoded fibers," *Opt. Express* **11**, 2838-2847 (2003).
3. K.S. Lee, and T. Erdogan, "Fiber mode conversion with tilted gratings in an optical fiber," *J. Opt. Soc. Am. A* **18**, 1176-1185 (2001).
4. S. Ramachandran, P. Kristensen, and M. Yan, "Generation and propagation of radially polarized beams in optical fibers," *Opt. Letters* **34**, 2525-2527 (2009)
5. Y. Yirmiyahu, A. Niv, G. Biener, V. Kleiner, and E. Hasman, "Excitation of a single hollow waveguide mode using inhomogeneous anisotropic subwavelength structures," *Opt. Express* **15**, 13404-13414 (2007).
6. A.F. Abouraddy, Q. Hu, O. Shapira, J. Viens, J.D. Joannopoulos, and Y. Fink, "Transmission of different angular-momentum modes in cylindrically symmetric photonic bandgap fibers in the near infrared," *CLEO 2007*.
7. T.G. Euser, G. Whyte, M. Scharrer, J.S.Y. Chen, A. Abdolvand, J. Nold, C.F. Kaminski, and P.St.J. Russell, "Dynamic control of higher-order modes in hollow-core photonic crystal fibers," *Opt. Express* **16**, 17972-17981 (2008).
8. B. Temelkuran, S.D. Hart, G. Benoit, J.D. Joannopoulos, and Y. Fink, "Wavelength-scalable hollow optical fibres with large photonic band gaps for CO<sub>2</sub> laser transmission," *Nature* **20**, 650-653 (2002).
9. K. Kuriki, O. Shapira, S.D. Hart, G. Benoit, Y. Kuriki, J.F. Viens, M. Bayindir, J.D. Joannopoulos, and Y. Fink, "Hollow multilayer photonic bandgap fibers for NIR applications," *Opt. Express* **12**, 1510-1517, (2004).
10. O. Shapira, K. Kuriki, N.D. Orf, A.F. Abouraddy, G. Benoit, J.F. Viens, M.M. Brewster, A. Rodriguez, M. Ibanescu, J.D. Joannopoulos, and Y. Fink, "Surface-Emitting Fiber Lasers," *Opt. Express* **14**, 3929-3935 (2006).
11. S. Johnson, M. Ibanescu, M. Skorobogatiy, O. Weisberg, T. Engeness, M. Soljacic, S. Jacobs, J.D. Joannopoulos, and Y. Fink, "Low-loss asymptotically single-mode propagation in large-core OmniGuide fibers," *Optics Express* **9**, 748-779 (2001).
12. John D. Joannopoulos, Steven G. Johnson, Joshua N. Winn, and Robert D. Meade, "*Photonic Crystals*," (Princeton University Press 2008).
13. O. Shapira, A.F. Abouraddy, J.D. Joannopoulos, and Y. Fink, "Complete Modal Decomposition for Optical Waveguides," *Phys. Rev. Lett.* **94**, 143902 (2005).
14. T. Engeness, M. Ibanescu, S. Johnson, O. Weisberg, M. Skorobogatiy, S. Jacobs, and Y. Fink, "Dispersion tailoring and compensation by modal interactions in OmniGuide fibers," *Opt. Express* **11**, 1175-1196 (2003).

## **Polymer-composite fibers for transmitting high peak power pulses at 1.55 microns**

### **Project Staff**

Zachary Ruff, Dana Shemuly, Ofer Shapira, Zheng Wang, and Yoel Fink

### **Sponsors**

ISN, NSF, ONR/Raydiance

Hollow-core photonic bandgap fibers (PBG) offer the opportunity to suppress highly the optical absorption and nonlinearities of their constituent materials, which makes them viable candidates for transmitting high-peak power pulses. We report the fabrication and characterization of polymer-composite PBG fibers in a novel materials system, polycarbonate and arsenic sulfide glass [1]. Propagation losses for the 60 $\mu$ m-core fibers are less than 2dB/m, a 52x improvement over previous 1D-PBG fibers at this wavelength. Through preferential coupling the fiber is capable of operating with over 97% the fiber's power output in the fundamental ( $HE_{11}$ ) mode. The fiber transmitted pulses with peak powers of 11.4 MW before failure.

High-peak power laser pulses in the near infrared (NIR) have important medical, industrial and military applications. In conventional single-mode silica fibers, the damage threshold due to the core material's finite optical absorption, and the pulse distortion induced by the core material's self-phase modulation limit the transmitted peak power. To reduce the optical power density in the core, large mode-area silica fibers have been developed, but poor-mode quality, peak-power limitations and coupling instabilities limit their suitability for many applications [2]. An alternative approach is to guide the pulse using a mirror or a photonic crystal, eliminating the core material. Large-core hollow fibers such as polymer-metal waveguides have been shown to transmit high-peak power pulses, but poor mode quality too restricts their performance [3]. Air-silica 2D-photonic crystal fibers (PCF) can deliver pulses without compromising mode-quality, though they can have a somewhat limited damage threshold, since even commercially optimized designs confine only ~98% of the transmitted power to the air-core of the fiber [4,5,9,11]. In this paper, we will show that 1D-PCF or photonic bandgap (PBG) fibers can strongly confine light to a hollow core, suppressing materials absorption and nonlinearities by over 5 orders of magnitude, while still delivering mode qualities approaching that of a step-index single mode fiber [6].

Earlier investigations into polymer-composite fibers used high temperature thermoplastics, such as polyethersulfone (PES) and polyetherimide (PEI) that have relatively high extinction coefficients compared to more common optical polymers. In this work, we demonstrate that optical polymers with lower extinction coefficients can be used to further reduce the absorption losses of PBG fibers. We chose polycarbonate over other amorphous optical polymers, such as Cyclic-Olefin copolymers, due to its commercial availability at experimentally favorable film thicknesses. Polycarbonate's extinction coefficient at 1.55 $\mu$ m is over an order of magnitude less than either PES's or PEI's coefficient, pushing the absorption loss limit for PBG fibers below 0.05 dB/m for a 60 $\mu$ m core fiber. Polycarbonate also exhibits low absorption into the visible spectrum, creating the opportunity for low-loss fibers with bandgaps approaching the UV. For this work, we were able only to source films extruded from a general use polycarbonate resin (Lexan 104), which contained significant inclusions (dust, poor molecular weight distribution). We expect an optical grade film to further improve transmission losses.

Scanning electron microscopy images are shown in fig. 1. The 760-micron outer diameter fiber has a 60-micron core ( $40\lambda$  at 1.5 $\mu$ m). The images show smooth interfaces between the glass and polymer layers. Fourier analysis on the SEM image of the 22 glass-polymer bilayers reveals a sharp peak at 521nm, agreeing strongly with our simulations. There is a tight distribution in the bilayer thickness with a full-width at half-maximum (FWHM) of 27nm, which is below the resolution of the SEM image.

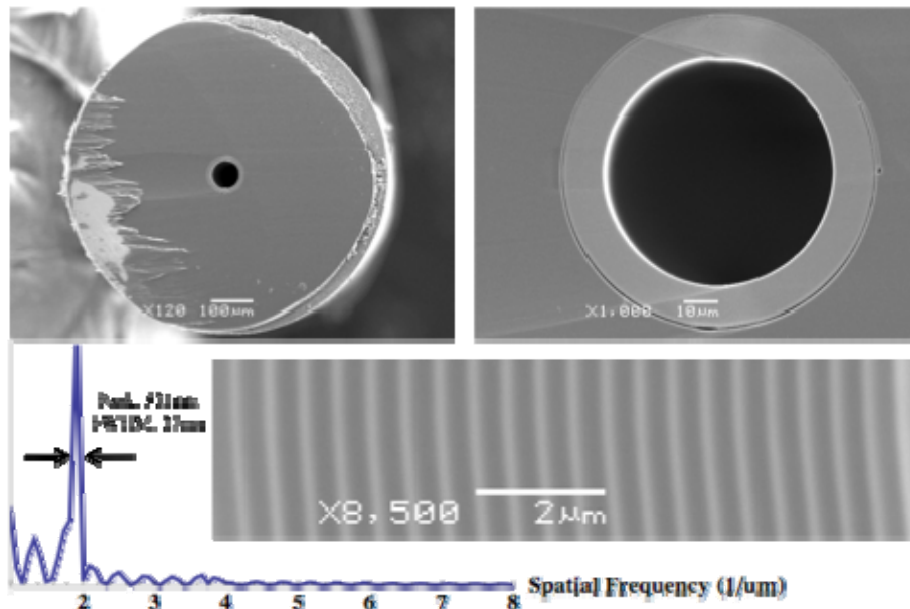


**Fig. 1:** Cross-sectional SEM images of a PBG fiber with a 60 $\mu\text{m}$ -core, a 760 $\mu\text{m}$  outer diameter and Fourier analysis of the glass-polymer bilayers

Propagation loss measurements were performed using the cutback method. The output of a single mode fiber coupled to a frequency-swept laser source from 1520nm-1620nm (Ando) provided a linear polarized Gaussian beam for the measurement. A spherical lens coupled the beam preferentially into the  $\text{HE}_{11}$  mode; the fiber's lowest order linearly polarized mode. A 2-meter section of fiber was held straight and cutback five times to 1-meter. Over the 100nm bandwidth of the laser, the propagation losses are from 2-3 dB/m, with a minimum loss of less than 2dB/m at 1560nm. The propagation losses are a significant improvement over previously published work of 5.5 dB/m for a 160 $\mu\text{m}$ -core fiber. Absorption and scattering losses scale as  $1/R^3$ , corresponding to a 52x improvement compared to the fiber in this work [8].

The modal content of the fiber's output was analyzed using a mode decomposition algorithm described in our previous work (fig. 2) [7]. Reducing the fiber's core-size limits modal coupling, since the spacing between modes scale as  $1/R^2$  [6]. Unlike previously demonstrated NIR fibers with larger cores, the modal content at the output of these fibers is over 97%  $\text{HE}_{11}$ . Since the  $\text{HE}_{11}$  mode overlaps strongly with a Gaussian beam, the fiber's output can be highly focused for applications where power density is critical. Another consequence of the increased mode spacing is that no additional bending losses were observed down to radii sufficient to damage the fiber mechanically ( $\sim 2\text{cm}$ ), when careful attention is paid to maintain the input coupling.

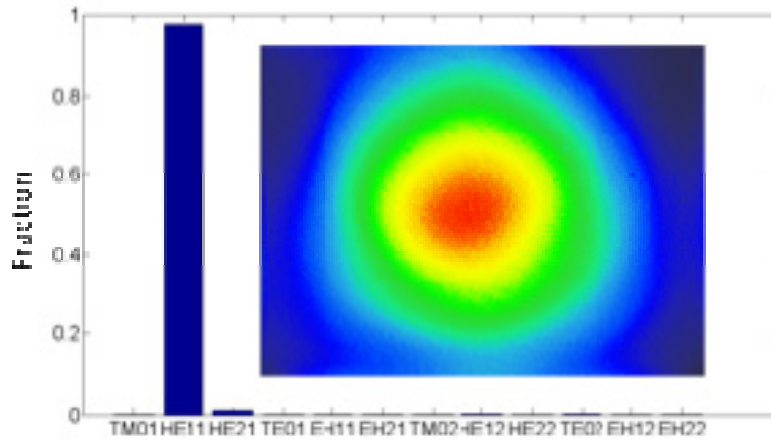


**Fig 2:** Far-Field intensity distribution at the output of the PBG fiber after 1-meter, excited at 1.55 $\mu$ m and the proportional modal content of the first 12 modes as determined by the modal-decomposition algorithm'

Despite these improvements, the fiber still exhibits propagation losses for the HE<sub>11</sub> mode two orders of magnitude greater than simulations that account for materials' absorption and the finite number of layers in the photonic crystal. An integrating sphere and detector were used to measure the power radiating from the fiber as the sphere was moved along the fiber. The radiation losses matched the propagation losses measured using the cutback technique. Therefore, scattering mechanisms such as interface roughness (air/core, bilayer) and inclusions (dust, phase separation) are likely limiting fiber performance and will be subject to further investigation. Each of these scattering mechanisms can potentially couple light from the HE<sub>11</sub> to either higher-order or cladding modes. Nonetheless, the high modal purity is maintained at the fiber's output due to a modal filtering mechanism where higher-order modes will have a higher differential loss than the fundamental mode [6].

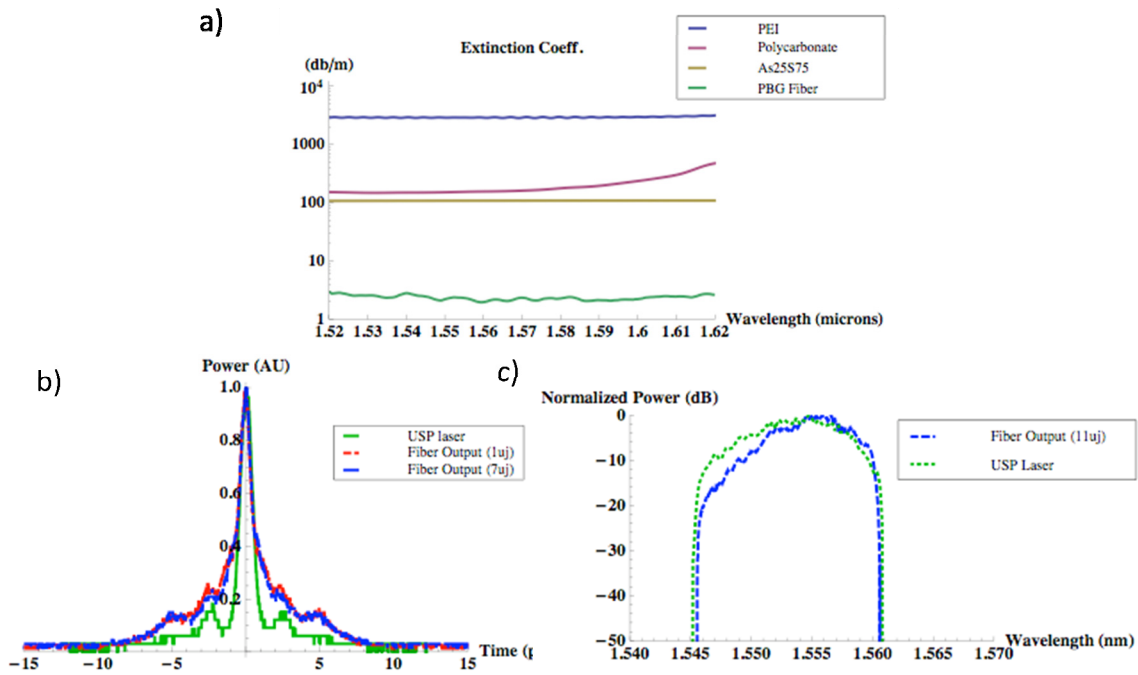


**Fig. 3:** (A) Extinction coefficients for materials and resultant fiber; all measurements were performed using the cutback method, (B) Autocorrelation traces of USP laser and fiber output, (C) OSA spectrum for the USP laser and the fiber output

Power handling measurements were performed using a laser source delivering 1-ps, 50 μJ pulses at 100 kHz centered at 1.552 μm (USP, Raydiance Inc.). The output of the laser was coupled to the fiber using a spherical lens. No additional beam shaping or end-facet protection, such as a ferrule or pinhole, was used. The input coupling efficiency was about 90% at low powers. The output of the PBG fiber was measured using an optical spectrum analyzer, an autocorrelator and power meter. A half-wave plate and polarizing beam-splitter were used to slowly increase the power coupled to the fiber until failure. Failure occurred at the end-facet at 12.7 μJ corresponding to a peak power of 11.4 MW and an average power of 1.14 W. The peak power was calculated by dividing the product of the coupling efficiency and the average power by the product of the pulse's temporal width (FWHM) and the repetition rate of the source. The  $HE_{11}$  mode of a 60 μm core fiber has a mode field diameter of 35 μm, corresponding to a power density of 1.2 TW/cm<sup>2</sup> in the fiber core. As the input power increased, there was no observable change in the pulse width or spectrum at the output of the fiber, suggesting non-linearities are not significant (fig. 3b-c). The fiber's dispersion was measured to be 9.6 ps-nm/km (OVA-Luna), which may account for the slight temporal broadening of the fiber's output with respect to the USP laser and appears to be independent of the input power.

To our knowledge, the highest reported peak-power for air-silica PCF fiber around 1.5 μm is 2.4 MW at atmosphere, using 110-fs pulses and a 12.7 μm core fiber [9]. We have not been able to find any studies that have determined the bulk damage threshold for silica at 1.55 μm for comparison. However, the bulk damage threshold for silica at 1.064 μm has recently been established to be in the 1.4 TW/cm<sup>2</sup> range for 14-ps pulses [10]. The damage threshold at the air-silica interface in solid-core silica fibers is considerably lower unless careful steps have been taken to completely eliminate surface roughness [10]. Simple 100 μm glass capillaries can transmit pulse with peak-powers over 10 TW, although their functionality is limited to transmission lengths of about 1 cm due to their relatively high propagation losses [12].

## References

1. Zachary Ruff, Dana Shemuly, Xiang Peng, Ofer Shapira, Zheng Wang, and Yoel Fink, "Polymer-composite fibers for transmitting high peak power pulses at 1.55 microns", *Opt. Express*, 18, 15697 (2010).
2. B. Richou, I. Schertz, I. Gobin, and J. Richou, "Delivery of 10-MW Nd:YAG laser pulses by large-core optical fibers: dependence of the laser-intensity profile on beam propagation," *Appl. Opt.* 36, 1610-1614 (1997).
3. Y. Matsuura, K. Hanamoto, S. Sato, and M. Miyagi, "Hollow-fiber delivery of high-power pulsed Nd:YAG laser light," *Opt. Lett.* 23, 1858 –1860 (1998).
4. S. Konorov, V. Mitrokhin, A. Fedotov, D. Sidorov-Biryukov, V. Beloglazov, N. Skibina, A. Shcherbakov, E. Wintner, M. Scalora, and A. Zheltikov, "Laser Ablation of Dental Tissues with Picosecond Pulses of 1.06- $\mu\text{m}$  Radiation Transmitted through a Hollow-Core Photonic-Crystal Fiber," *Appl. Opt.* 43, 2251-2256 (2004).
5. NKT Photonics. Data sheet. <http://www.nktpotonics.com/>, Accessed November 2009.
6. S. G. Johnson, M. Ibanescu, M. Skorobogatiy, O. Weisberg, T. D. Engeness, M. Soljacic, S. A. Jacobs, J. D. Joannopoulos, and Y. Fink "Low-loss asymptotically single-mode propagation in large-core OmniGuide fibers," *Opt. Express* 9, 748-779 (2001)
7. V. Nguyen, F. Sanghera, B. Cole, P. Pureza, F.H. Kung, I. D. Aggarwal. "Fabrication of Arsenic Sulfide Optical Fiber with Low Hydrogen Impurities". *J. Am. Ceram. Soc.*, 85 [8] 2056 –58 (2002)
8. Mendez and Morse. *Specialty Optical fibers handbook*. Elsevier. 2007
9. D. G. Ouzounov, F. R. Ahmad, D Müller, N. Venkataraman, M. T. Gallagher, M. G. Thomas, J. Silcox, K. W. Koch, A. L. Gaeta\* "Generation of Megawatt Optical Solitons in Hollow-Core Photonic Band-Gap Fibers". *Science*. 1702 (2003); 301
10. A. V. Smith, B. T. Do, "Bulk and surface laser damage of silica by picosecond and nanosecond pulses at 1064 nm," *Appl. Opt.* 47, 4812-4832 (2008),
11. J. D. Shephard, F. Couny, P. J. Russell, J. D. C. Jones, J. C. Knight, and D. P. Hand, "Improved hollow-core photonic crystal fiber design for delivery of nanosecond pulses in laser micromachining applications," *Appl. Opt.* 44, 4582-4588 (2005)
12. M. Borghesi, A. J. Mackinnon, R. Gaillard, O. Willi, and A. A. Offenberger, "Guiding of a 10-TW picosecond laser pulse through hollow capillary tubes," *Phys. Rev. E* 57, R4899–R4902 (1998)

## Resolving Optical Illumination Distributions along an Axially Symmetric Photodetecting Fiber

### Project Staff

Fabien Sorin, Guillaume Lestoquoy, Sylvain Danto, John D. Joannopoulos and Yoel Fink

### Sponsors

ARO, DARPA, ISN, NSF

Optical fibers rely on translational axial symmetry to enable long distance transmission. Their utility as a distributed sensing medium [1-3] relies on axial symmetry breaking either through the introduction of an a priori axial perturbation in the form of a bragg gratings [4], or through the use of optical time (or frequency) domain reflectometry techniques [5,6] which measure scattering from an adhoc axial inhomogeneity induced by the incident excitation. These have enabled the identification and localization of small fluctuations of various stimuli such as temperature [7-9] and stress [10-11] along the fiber axis. Due to the inert properties of the silica material the only excitations that could be detected were the ones that led to structural changes, importantly excluding the detection of radiation at optical frequencies. Recently, a variety of approaches have been proposed to integrate different materials inside optical fibers [12-20]. In particular, multimaterial fibers with metallic and semiconductor domains have offer the possibility to broaden the scope of detectable excitations to radiation at optical frequencies [19-24], over unprecedented length and surface area. Several applications have been proposed for these fiber devices in imaging [23,24], industrial monitoring [25,26], remote sensing and smart fabrics [20,21].

So far however, the challenges associated with resolving the intensity distribution of optical excitations along the fiber axis have not been addressed. Here we propose an approach that allows extraction of axially resolved information in a fiber that is uniform along its length without necessitating fast electronics. We design optoelectronic fibers with a specific geometry that supports a convex potential profile in order to break their axial uniformity. We then proceed to construct a hybrid solid-core/thin-film cross-sectional structure that allows us to impose and vary convex electrical potential profiles along a thin-film photodetecting fiber. We show how we can localize a point of illumination along a one-meter-long photodetecting fiber axis with a sub-centimeter resolution, and how the width of the incoming beam and the generated photoconductivity can also be measured. Finally, we show how two and three such beams simultaneously incident on an optoelectronic fiber can be locally resolved.

Photodetecting fibers typically comprise a semiconducting chalcogenide glass contacted by metallic electrodes and surrounded by a polymer matrix [19-21]. These materials are assembled at the preform level and subsequently thermally drawn into uniform functional fibers of potentially hundreds of meters in length, as illustrated in Fig. 1(A1). An electric potential  $V(z)$  across the semiconductor can be imposed along the fiber length by applying a potential drop  $V_0$  at one end as depicted in Figure 1(A2). As a result, a linear current density  $j_{dark}$  is generated in the semiconductor in the dark, between the electrodes. When an incoming optical wave front with an arbitrary photon flux distribution  $\Phi_0(z)$  is incident on a fiber of total length  $L$ , the conductivity is locally changed and a photo-current (total current measured minus the dark current) is generated due to the photoconducting effect in semiconductors, as illustrated in Figure 1(A2). The measured photo-current in the external circuitry is the sum of the generated current density  $j_{ph}(z)$  along the entire fiber length:  $i_{ph} = C \int_0^L V(z) \sigma_{ph}(z) dz$ , where  $C$  depends on the materials and geometry and is uniform along the fiber axis, and  $\sigma_{ph}$  is the locally generated film photo-conductivity that depends linearly on  $\Phi_0(z)$  in the linear regime considered [22-24,30-32]. Note that for simplicity the integrations on the other cylindrical coordinates  $r$  and  $\theta$  are not represented. Also, we neglect the diffusion of free carriers along the fiber axis since it would occur over the order of a micrometer, several orders of magnitude lower than the expected resolution (millimeter range).

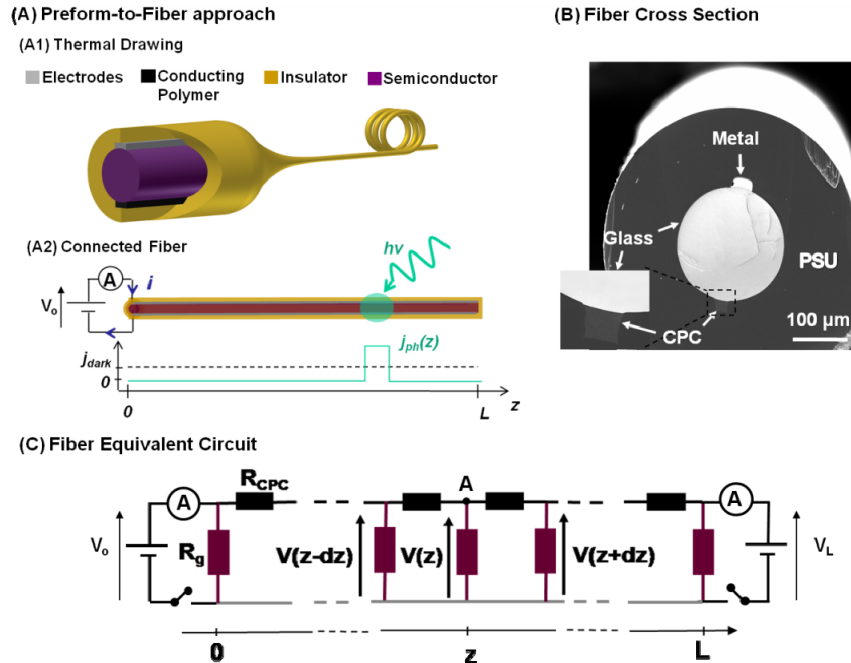


**Fig. 1:** A(1). 3D Schematic of the multimaterial fiber thermal drawing fabrication approach. A(2). Schematic of a connected photodetecting fiber with an illumination event. The graph represents the linear current density in the dark and under the represented illumination. B. Scanning Electron Microscope micrograph of the fiber cross-section (inset: zoom-in on the contact between the core and the CPC electrode); C. Schematic of the fiber system's equivalent circuit.

For the photodetecting fibers considered so far, the conductivity of the semiconductor in the dark and under illumination has been orders of magnitude lower than the one of the metallic electrodes. These electrodes could hence be considered equipotential, and  $V(z) = V_0$  along the fiber axis  $z$  over extend lengths. As a result,  $j_{dark}$  is also uniform as depicted on the graph in Figure 1(A2). Moreover, the photo-current measured in the external circuitry integrates the photo-conductivity distribution  $\sigma_{ph}(z)$  along the fiber length. This single, global current measurement does not contain any local information about the incident optical intensity distribution along the fiber axis. In particular, even the axial position of a single incoming optical beam could not be reconstructed. To alleviate this limitation, we propose an approach that breaks the axial symmetry of this fiber system and enables to impose various non-uniform electric potential distributions along the fiber axis. By doing so, we can generate and measure several global photo-currents  $i_{ph}$  where the fixed and unknown distribution  $\sigma_{ph}(z)$  is modulated by different known voltage distributions  $V(z)$ . We will then be able to access several independent photo-current measurements from which information about the intensity distribution along the fiber axis will be extracted, as we will see.

To controllably impose a non-uniform electrical potential profile  $V(z)$ , we propose to replace one (or both) metallic conducts by a composite material that has a higher electrical resistivity. This electrode, or resistive channel, can no longer be considered equipotential and a non-negligible drop of potential will occur not only accross the semiconductor but also along the fiber axis. An ideal material for this resistive channel was found to be a composite polymer recently successfully drawn inside multimaterial fibers [27], that embeds Carbon black nanoparticles inside a Polycarbonate matrix (hereafter: conducting polycarbonate or CPC) [28]. The CPC resistivity,  $\rho_{CPC}$  (1-10  $\Omega.m$  as measured post-drawing), lies in-between the low resistivity of metallic elements (typically  $10^{-7}$   $\Omega.m$ ) and the high resistivity of chalcogenide glasses (typically  $10^6$ - $10^{12}$   $\Omega.m$ ) used in multimaterial fibers. It is very weakly dependant on the optical radiations considered so that it will not interfere with the detection process.

To validate this approach we first demonstrate the drawing compatibility of these materials. We fabricated a photodetecting fiber with a semiconducting chalcogenide glass core (of composition  $\text{As}_{40}\text{Se}_{50}\text{Te}_{10}$ ) contacted by one metallic electrode ( $\text{Sn}_{63}\text{Pb}_{37}$ ) and by another conduct made out of the proposed CPC composite. A Scanning Electron Microscope (SEM) micrograph of the resulting fiber cross-section is shown in Fig. 1B that demonstrate the excellent cross-sectional features obtained. To first theoretically analyze this new system, we depict its equivalent circuit in Fig. 1C. The semiconducting core can be modelled as multiple resistors in parallel, while the CPC channel is comprised of resistors in series. To find the voltage distribution  $V(z)$  in this circuit, we can apply Kirchoff's laws at point A:

$$\frac{V(z) - V(z - dz)}{R_{CPC}} = \frac{V(z + dz) - V(z)}{R_{CPC}} - \frac{V(z)}{R_g}, \text{ or } \frac{\partial^2 V}{\partial z^2} = \frac{R_{CPC}}{R_g dz^2} V(z) \quad (1)$$

or simply:

$$\frac{\partial^2 V}{\partial z^2} = \frac{V(z)}{\delta(z)^2} \quad (2)$$

with

$$\delta(z) = \sqrt{\frac{\rho_g(z)}{\rho_{cpc}} \frac{\pi}{2} S_{cpc}} \quad (3)$$

where  $R_{CPC}$  is the resistance of the CPC channel over an infinitesimal distance  $dz$  ( $R_{CPC} = \rho_{CPC} dz / S_{CPC}$ ),  $S_{CPC}$  being the surface area of the CPC electrode in the fiber cross-section. Similarly,  $R_g$  is the resistance of a slab of cylindrical semiconducting core of length  $dz$  that can be derived by considering a point contact between the electrodes and the solid-core, ( $R_g(z) = \pi \rho_g(z) / (2dz)$ , with  $\rho_g$  the glass resistivity). The new parameter  $\delta$  has the dimensionality of a length and is referred to as the characteristic length of the fiber system. It can be tuned by engineering the glass composition (hence changing  $\rho_g$ ), as well as the structure and geometry of the fiber.

Two sets of boundary conditions depicted in Fig. 2 can be defined for this system: BC(1) where one fiber end ( $z = 0$  or  $L$ ) is brought to a potential  $V^{BC(1)}(0) = V_0$  while the other ( $z = L$  or  $0$ ) is left floating, resulting in  $\partial V^{BC(1)}(L) / \partial z = 0$  since no accumulation of charges is expected; and BC(2) where we apply a voltage at both fiber ends,  $V^{BC(2)}(0) = V_0$  and  $V^{BC(2)}(L) = V_L$ . The two potential profiles can then be derived when  $\delta$  is independent of  $z$ , and are given by two *convex* functions:

$$V^{BC1}(z) = \frac{V_0 \cosh\left(\frac{L-z}{\delta}\right)}{\cosh\left(\frac{L}{\delta}\right)} \quad (4)$$

$$V^{BC2}(z) = \frac{V_0 \sinh\left(\frac{L-z}{\delta}\right) + V_L \sinh\left(\frac{z}{\delta}\right)}{\sinh\left(\frac{L}{\delta}\right)} \quad (5)$$

To assess our model, we fabricated three fibers with different materials and structures. All fibers have one metallic electrode ( $\text{Sn}_{63}\text{Pb}_{37}$  alloy) and one CPC electrode of same size. Two fibers have a solid-core structure like the one shown in Fig. 1B, with two different glass compositions from the chalcogenide system As-Se-Te,  $\text{As}_{40}\text{Se}_{50}\text{Te}_{10}$  (AST<sub>10</sub>) and  $\text{As}_{40}\text{Se}_{42}\text{Te}_{18}$  (AST<sub>18</sub>). The third fiber has a thin-film structure with a 500 nm layer of  $\text{As}_{40}\text{Se}_{50}\text{Te}_{10}$  [22,24]. This thin film structure is expected to have a very large characteristic length since its conductance is many orders of magnitude lower than the one of both metallic and CPC electrodes. In solid-core fibers however,  $\delta$  should be of the order of the fiber length, inducing a significant variation in the potential profile. Separate measurement of the CPC electrode resistivity ( $\rho_{CPC} = 1.4 \Omega.m$  and  $\rho_{CPC} = 1.2 \Omega.m$  in pieces from the AST<sub>10</sub> and AST<sub>18</sub> fibers respectively) and the glass conductivities lead to expected  $\delta$  values of 40 cm and 9 cm in the AST<sub>10</sub> and AST<sub>18</sub> fibers respectively, the higher conductivity of AST<sub>18</sub> being responsible for the lower  $\delta$  parameter [33].

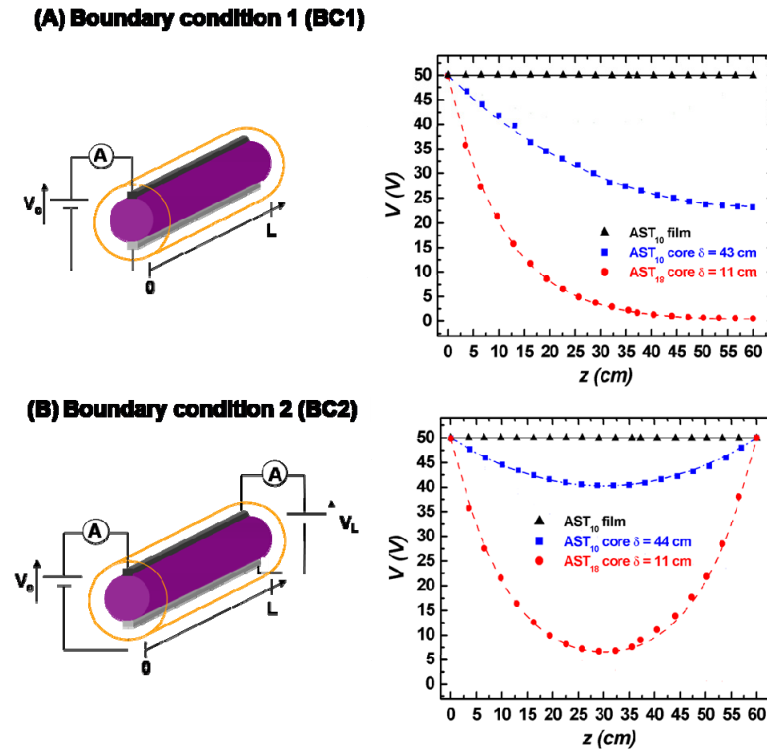


**Fig. 2:** (A) Schematic of the fiber contact for boundary conditions (1) and graph representing the experimental results (dots) and the fitted theoretical model (lines) of the voltage profile between the CPC electrode and the metallic conduct at different points along the fiber axis, when the fiber is under BC(1) and for different fibers: in black,  $AST_{10}$  thin-film; in blue,  $AST_{10}$  core and in red,  $AST_{18}$ . (B) Same as (A) but when the fiber is under BC(2)

We then cut a 60-cm-long piece from each fiber and made several points of contact on the CPC electrodes while contacting the metallic conduct at a single location. We applied a 50 V potential difference for both BC(1) and BC(2), and measured the potential drop between the contact points along the CPC channel and the equipotential metallic conduct, using a Keithley 6517A multimeter. The experiment was performed in the dark to ensure the uniformity of  $\delta$ . The results are presented in Fig. 2 where the data points are the experimental measurements while the curves represent the theoretical model derived above, fitted over  $\delta$ . As we expected, the thin-film fiber maintains a uniform potential along its axis. For solid-core fibers, the fitting values (43 cm and 11 cm for BC(1), and 44 cm and 11 cm for BC(2) for  $AST_{10}$  and  $AST_{18}$  fibers respectively) match very well with the expected  $\delta$  parameters. The discrepancy is due to errors in measuring the different dimensions in the fiber, and potential slight non-uniformity of the glass conductivity due to local parasitic crystallization during the fabrication process [34]. Noticeably, the  $\delta$  values obtained for both boundary conditions are in excellent agreement, which strongly validates our model.

Solid core fibers can hence support convex potential profiles that can be tuned using different glass compositions or fiber structure. When an optical signal is impingent on the fiber however,  $\delta$  is no longer uniform as we considered earlier, since the glass resistivity is locally changed. This will in turn affect  $V(z)$  that becomes an unknown function of the intensity distribution of the optical wave front. Moreover, thin-film structures are a more attracting system to work with in light of their better sensitivity and other advantages described in ref. [22]. To address these observations we propose an hybrid structure that enables to impose convex potential distributions that remain unchanged under illumination, across a semiconducting thin-film that is used as the higher sensitivity detector. The fiber cross-section is shown in Fig. 3A, where a CPC electrode contacts

both a solid-core and a thin-film structure. The equivalent circuit is represented in Fig. 3C, where one can see that the two systems are in parallel. The drop of potential between the CPC channel and the metallic electrodes (both at the same potential) expressed in Eq. 1 now becomes:  $V(1/R_c + 1/R_f)$ , where  $R_c$  and  $R_f$  are the resistance of a slab of cylindrical semiconducting solid-core and thin-film respectively, of length  $dz$ . This leads to a new differential equation:

$$\frac{\partial^2 V}{\partial z^2} = V\left(\frac{1}{\delta_c^2} + \frac{1}{\delta_f^2}\right) \approx \frac{V}{\delta_c^2} \quad (6)$$

since  $\delta_c$  and  $\delta_f$ , the characteristic parameters for the solid-core and the thin-film respectively, verify  $\delta_c \ll \delta_f$  as can be anticipated from earlier results. The potential distribution is hence imposed by the solid-core system, while the current flowing through the photoconducting film can be measured independently, thanks to the different metallic electrodes contacting the solid-core and the thin-film structures. Similar boundary conditions can be imposed to the solid-core sub-system as before.

To verify our approach we fabricated a fiber integrating a structure with a CPC electrode in contact with both a solid-core of  $As_{10}$  and a thin layer of the  $As_{40}Se_{52}Te_8$  glass. This glass composition was chosen for its better thermal drawing compatibility with the polysulfone (PSU) cladding used here, which results in a better layer uniformity. Note that in this fiber, the metallic electrodes were embedded inside a CPC electrode. The conductivity of this assembly is still dominated by the high conductivity of the metal. The high viscosity of CPC in contact with the thin-film is however beneficial to maintain a layer of uniform thickness [35]. The contacts between the CPC electrodes and the glasses were found to be ohmic.

We reproduced the experiment described above to measure the potential drop between the CPC and the metallic electrodes along a one-meter long fiber piece. This time however, the experiment was done under three conditions: first in the dark, then when the fiber was illuminated, at the same location, by a white light source and then by a green (532 nm) LED of similar intensity. The results are shown in Fig. 3B and illustrate the proposed concept very well. Since the green light is almost fully absorbed in the semiconducting layer [24],  $\delta_c$  and thus the potential distribution across the layer, remain unchanged. White light on the other hand penetrates much deeper in the material and reaches the solid-core, changing  $\delta_c$  and hence the voltage distribution. From these experiments we could extract the value  $\delta_c = 143$  cm for this fiber system. This value is much larger than measured before due to the increase of  $S_{CPC}$  imposed by the new structure design. Note that we used green versus white light for this proof of concept, but many fiber parameters such as the glass composition or fiber geometry can be tuned to apply this approach to a wide range of radiation frequencies.

Our new fiber system can now support a fixed potential profile  $V(z)$  that can be varied by changing the applied boundary conditions. Given the linear relation of hyperbolic functions that appear in the convex potential profiles derived in Eq. (3), one realizes that all possible profiles are a linear combination of the two functions:

$$V^I(z) = \frac{V}{\sinh(L/\delta_c)} \sinh\left(\frac{L-z}{\delta_c}\right) \quad (7)$$

and 
$$V^{II}(z) = \frac{V}{\sinh(L/\delta_c)} \sinh\left(\frac{z}{\delta_c}\right) \quad (8)$$

obtained for the boundary conditions  $V_0 = V$  and  $V_L = 0$ , and vice versa. A third independent voltage profile can also be imposed by applying a voltage between the CPC electrode and the electrode contacting the thin-film only, resulting in a nearly uniform potential  $V^{III}(z) = V$ , since  $\delta_f$  is much larger than the fiber lengths considered. Hence, we can measure three independent photo-currents that result from the integration of the stimuli intensity profile modulated by these

different voltage distributions, from which some axial information about  $\sigma_{ph}$  and hence  $\Phi_0$  can be extracted as we show below.

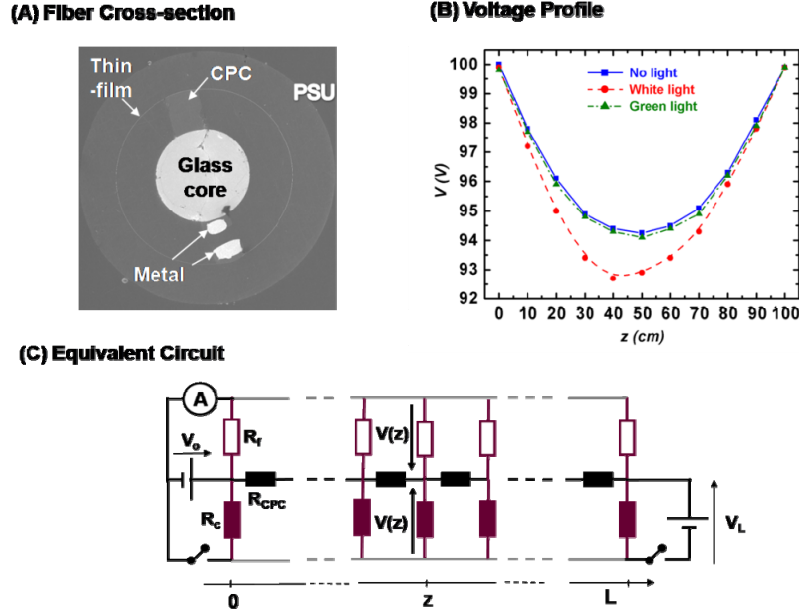


**Fig. 3:** A: SEM micrograph of a fiber with the new thin-film/solid-core structure. B: Experimental results (dots, the lines are added for clarity) of the voltage profile of a one-meter long fiber piece from panel A in the dark (in blue), and under a spot of white light (in red) and green light (in green) at the same location, same width and of similar intensity. C: schematic of the electrical connection to one fiber end.

Let us consider the case of an incident uniform light beam, with a rectangular optical wave front, at a position  $z_0$  along the fiber axis, and with a width  $2\Delta z$ . It generates a photo-conductivity profile  $\sigma_{ph}(z) = \sigma_{ph}$  if  $z \in [z_0 - \Delta z, z_0 + \Delta z]$ , and 0 otherwise. The generated current for each configuration can be derived, integrating over the illumination width and re-arranging the hyperbolic terms:

$$i_{ph}^I = \frac{2CV\sigma_{ph}}{\sinh(L/\delta_c)} \sinh\left(\frac{L-z_0}{\delta_c}\right) \sinh\left(\frac{\Delta z}{\delta_c}\right) \quad (9)$$

$$i_{ph}^{II} = \frac{2CV\sigma_{ph}}{\sinh(L/\delta_c)} \sinh\left(\frac{z_0}{\delta_c}\right) \sinh\left(\frac{\Delta z}{\delta_c}\right), \quad (10)$$

$$i_{ph}^{III} = 2CV\sigma_{ph}\Delta z \quad (11)$$

Remarkably, the first two currents are a function of the beam position which can be simply extracted by taking the ratio  $r = i_{ph}^I / i_{ph}^{II}$ , alleviating the dependence on the beam intensity and width. We can extract  $z_0$  from the measurement of  $r$  through the relation:

$$z_0 = \frac{\delta_c}{2} \ln \left[ \frac{e^{L/\delta_c} + r}{e^{-L/\delta_c} + r} \right] \quad (12)$$

This was experimentally verified by illuminating a one-meter long piece of the fiber shown in Fig. 3, with a 1 cm width beam from a green LED, at different locations along the fiber length. The results are shown in Fig. 4A where the straight line represents the experimental points of illumination of the fiber while the dots are the reconstructed positions from measuring the ratio of photo-currents  $r$ . The agreement between the experimental and measured positions is excellent, with errors made on the position smaller than  $\pm 0.4$  cm in the middle of the fiber.

Error over the beam position depends on a large number of parameters (Fiber length,  $\delta_c$ , beam position and intensity, geometry etc...). Indeed, fluctuations of the photo-currents, that

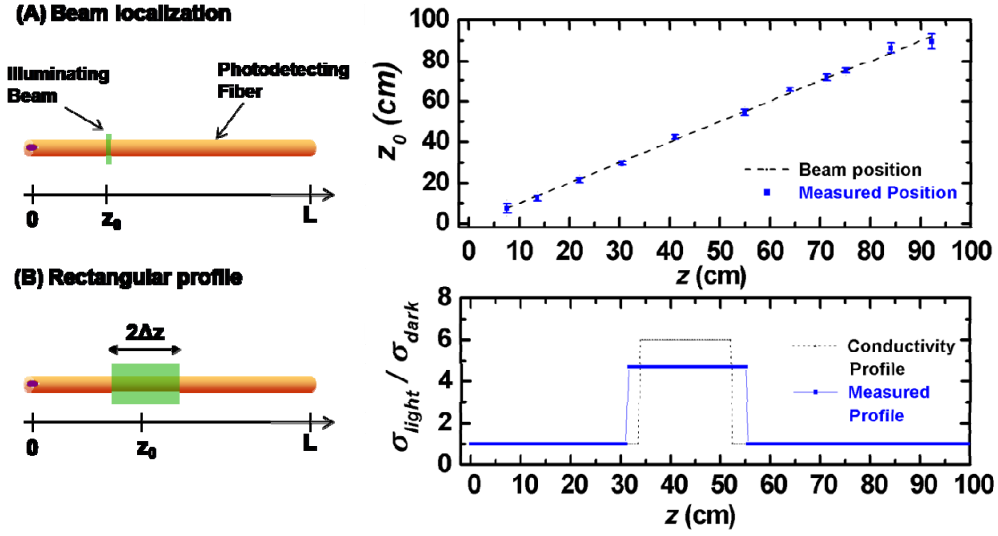


**Fig. 4:** Schematic of the illuminated fiber by a single optical beam and graph of the real position (black dashed line) and reconstructed position with error bars (blue dots) of an optical beam incident on a 1 m-long fiber at different positions. (B) Schematic of the illuminated fiber by a rectangular optical wave front. And graph of the real profile (black dotted line) and reconstructed profile (blue dots) of a rectangular wave front incident on the same fiber.

come from various sources [30-32], lead to variations on the ratio  $r$ , resulting in errors in the measured beam's position. To assess the resolution of our system, we first measured the dark current noise  $i_N$ , considered in good approximation to be the only source of noise here. We found it to be around 10 pA in our experimental conditions, using similar techniques as those explained in ref. [22]. This noise current is the same for configurations I and II given the symmetry of the system. Intuitively, when one measures a photo-current  $i_{ph}^{I,II}$ , its mean value lies within the segment defined by  $i_{ph}^{I,II} \pm i_N$ . In a simple and conservative approach, we define the resolution of our system as the difference  $z_{0+} - z_{0-}$  of the two obtained positions  $z_{0+}$  and  $z_{0-}$  when the maximum error on the currents are made, i.e. when  $r$  is given by  $r_+ = (i_{ph}^I + i_N) / (i_{ph}^{II} - i_N)$  and  $r_- = (i_{ph}^I - i_N) / (i_{ph}^{II} + i_N)$  respectively. These error bars are represented in the graph of Fig. 4A. The resolution found is sub-centimeter, corresponding to two orders of magnitude smaller than the fiber length. This is to the best of our knowledge the first time that a beam of light can be localized over such an extended length and with such a resolution, using a single one dimensional distributed photodetecting device requiring only four points of electrical contact.

The beam position is not the only spatial information we can reconstruct with this system. Indeed, the ratio of  $i_{ph}^{II}$  and  $i_{ph}^{III}$  allows us to reconstruct  $\Delta z$  as  $z_0$  is known, by measuring the ratio  $\sinh(\Delta z / \delta_c) / (\Delta z / \delta_c)$ . This also enables to evaluate  $\sigma_{ph}$ , using  $i_{ph}^{III}$ . In Fig. 3B we show the experimental illumination profile of a green LED light (black dashed line, centered at 43 cm, width 18 cm, with a conductivity  $\sigma_{ph} = 6 \sigma_{dark}$ ) and the reconstructed profile from current measurements (blue data points, centered at 43.5 cm, width 24 cm and  $\sigma_{ph} = 4.7 \sigma_{dark}$ ). The positioning is very accurate as expected from the results above, while a slightly larger width is measured. This error is due to the large value of  $\delta_c$  compared to  $\Delta z$ , which results in a ratio of  $i_{ph}^{II}$  to  $i_{ph}^{III}$  more sensitive to noise than the ratio of  $i_{ph}^I$  over  $i_{ph}^{II}$ . It is however clear from discussions above that the fiber system can be designed to have a much better resolution for different beam width ranges, by tuning  $\delta_c$  to smaller values.

Also under study is the integration time required for this system. The speed at which we can vary the potentials depends on the bandwidth associated with the equivalent circuit, taking into account transient current effects in amorphous semiconductors. In this proof-of-concept, measurements were taken under DC voltages applied, varying the boundary conditions after transient currents are stabilized (typically after a few seconds). Novel designs, especially fibers

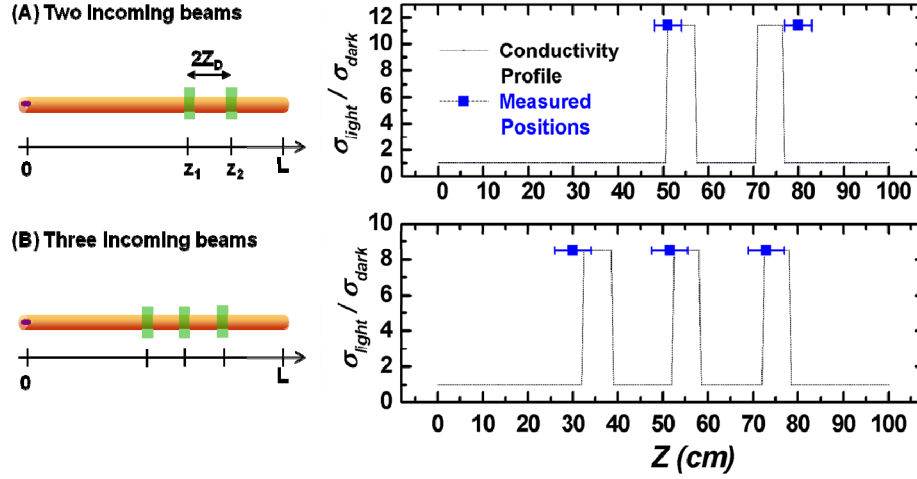


**Fig. 5:** (A) Schematic: photodetecting fiber illuminated by two similar optical beams. Graph: position measurements of the two beams. In black dotted line is the conductivity profile generated by the two incoming beams while the blue dots are the reconstructed positions with the error bars. (B) Schematic: photodetecting fiber illuminated by three similar optical beams. Graph: position measurements of the three beams. In black dotted line is the conductivity profile generated by the three incoming beams while the blue dots are the reconstructed positions with the error bars.

where the semiconducting material has been crystallized through a post-drawing crystallization process [14], and integrating rectifying junctions that have proven to have several kHz of bandwidth [15], could result in significant improvement in device performance and speed.

With this novel approach, several beams simultaneously incident on the fiber can also be addressed given that some prior knowledge on their distribution is known. Especially, we only need to know that the beams have a width much smaller than the solid-core characteristic length  $\delta_c$  (so that  $\sinh(\Delta z/\delta_c)/(\Delta z/\delta_c) \approx 1$ ) to localize two such beams incoming at arbitrary locations on the fiber. Indeed, let us consider two similar beams of width  $2\Delta z$  (with  $\Delta z \ll \delta_c$ ) generating a photo-conductivity  $\sigma_{ph}$  at two arbitrary positions  $z_1$  and  $z_2$  (with  $z_1 < z_2$ ) on the fiber. The photo-currents measured are the sum of the measured currents with individual beams. Defining  $Z_m = \frac{z_1 + z_2}{2}$  and  $Z_D = \frac{z_2 - z_1}{2}$ , we can derive:

$$i_{ph}^I = \frac{4CV\sigma_{ph}}{\sinh(L/\delta_c)} \sinh\left(\frac{\Delta z}{\delta_c}\right) \sinh\left(\frac{L-Z_m}{\delta_c}\right) \cosh\left(\frac{Z_D}{\delta_c}\right) \quad (13)$$

$$i_{ph}^{II} = \frac{4CV\sigma_{ph}}{\sinh(L/\delta_c)} \sinh\left(\frac{\Delta z}{\delta_c}\right) \sinh\left(\frac{Z_m}{\delta_c}\right) \cosh\left(\frac{Z_D}{\delta_c}\right) \quad (14)$$

$$i_{ph}^{III} = 4CV\sigma_{ph}\Delta z \quad (15)$$

Following the same approach as in the single beam case, we can reconstruct  $Z_m$  and  $Z_D$ , and hence  $z_1$  and  $z_2$ . On Fig. 5A, we show the experimental illumination of a fiber with two identical

beams of width 6 cm from the same green LED (dashed black curve) at positions 54 cm and 75 cm. The blue dots represent the reconstructed beam position, with measured position  $51 \pm 3$  cm and  $78 \pm 3$  cm for the two beams. The error on the positions were computed in a similar fashion as before.

An optical signal made out of three beams requires additional constraints to be resolved. For example, three similar beams equidistant from one another can be detected and localized with our system. Indeed, here again only two unknowns have to be found: the central beam position and the distance between two adjacent beams. The derivation of the algorithm to extract these positions from the different current measurements is very similar to what has been derived above. In Fig. 5B we show experimental results of the localization of three incoming beams of same width ( $\Delta z = 6$  cm) and intensity (generating a photo-conductivity  $\sigma_{ph} = 8.5\sigma_{dark}$ ) at positions  $z_1 = 35.5$  cm,  $z_2 = 55.5$  cm, and  $z_3 = 75.5$  cm. The generated conductivity pattern is represented by a black dotted line on the graph. The reconstructed positions from photo-current measurements were  $30 \pm 4$  cm,  $51.5 \pm 4$  cm and  $73 \pm 4$  cm, in very good agreement with the real beams locations.

In conclusion, we have designed a novel fiber structure that combines a conducting polymer composite in contact with a thin-film and a solid-core glass, each contacted by a different metallic electrode. We were able to break the axial uniformity of the voltage distribution and generate convex potential profiles along the fiber axis that can be varied by changing the boundary conditions. We demonstrated that we could reconstruct the position, width and the generated photoconductivity of an arbitrary incoming rectangular optical wavefront. Under given constraints, two and three simultaneously incident beams could also be spatially resolved.

The ability to localize various stimuli along extended fiber length using simple electronic measurement schemes and with limited electrical connections, significantly impacts multimaterial fiber sensor performance. Among many examples, defects in self-monitored optical fibers could not only be detected but also localized [25]. Fiber-based lensless imaging grids and fabrics [23,24] would require simpler or no back projection algorithm procedure to extract a 2D intensity pattern. Indeed, a pattern like the letter E in ref [24] incident on the fiber grid is made out of optical wave fronts with rectangular profiles incident on each fiber. These patterns could be reconstructed with the new system presented here, without the inconvenient step of rotating the object to perform the back projection algorithm, significantly improving the practicality of the proposed fiber-based lensless imaging approach.

Finally, the concepts introduced here address in an original way the fundamental challenge of “pixellizing” a distributed sensor. The results on localizing optical intensity variations over long distances resemble the pioneering work reported on distributed temperature sensing using optical fibers in ref. [7-9], that led to the important developments of today’s fiber optic sensing technology. New ways to address the fiber and measure more independent photo-currents are under study to enable the reconstruction of increasingly complex optical wave fronts, paving the way towards distributed light sensing.

## References

1. F. Yu, S. Yin, *Fiber Optic Sensors*, Marcel-Dekker, (2008).
2. K.T.V. Grattan and B.T. Meggitt, Editors, *Optical Fiber Sensor Technology, Fundamentals*, Kluwer Academic Publishers, Boston (2000).
3. A. Rogers, “Distributed optical-fiber sensing”, *Meas. Sci. Technol.* **10**, R75 (1999).
4. A. Othonos and K. Kalli. *Fiber Bragg Gratings—Fundamentals and Applications in Telecommunications and Sensing*, Artech House, Boston (1999).
5. M. K. Barnoski and S. M. Jensen, “Fiber waveguides: a novel technique for investigating attenuation characteristics”, *Applied Optics* **15**, 2112 (1976).
6. A. J. Rogers, “Polarization optical time domain reflectometry: a technique for the measurement of field distributions”, *Applied Optics*, **20** 1060 (1981).

7. A. H. Hartog, "A distributed temperature sensor based on liquid-core optical fibers", *IEEE J. Light. Tech.*, **1**(3), 498 (1983).
8. J. P. Dakin, D. J. Pratt, G. W. Bibby, J. N. Ross, "Distributed optical fiber raman temperature sensor using a semiconductor light source and detector", *Elec. Lett.*, **21**, 569 (1985)
9. T. Kurashima, T. Horiguchi, and M. Tateda, "Distributed-temperature sensing using stimulated Brillouin scattering in optical silica fibers" *Opt. Lett.*, **15**, 1038 (1990).
10. C. I. Merzbachery, A. D. Kersey and E. J. Friebele, "Fiber optic sensors in concrete structures: a review", *Smart Mater. Struct.* **5**, 196 (1996).
11. X. Bao, D. J. Webb, D. A. Jackson, "Combined distributed temperature and strain sensor based on Brillouin loss in an optical fiber", *Opt. Lett.* **16**, 141 (1994).
12. P. J. A. Sazio, A. Amezcua-Correa, C. E. Finlayson, J. R. Hayes, T. J. Scheidemantel, N. F. Baril, B. R. Jackson, D. J. Won, F. Zhang, E. R. Margine, V. Gopalan, V. H. Crespi, J. V. Badding, "Microstructured Optical Fibers as High-Pressure Microfluidic Reactors", *Science* **311**, 1583 (2006).
13. T. T. Larsen, A. Bjarklev, D. S. Hermann, and J. Broeng, "Optical devices based on liquid crystal photonic bandgap fibres," *Opt. Exp.* **11**, 2589 (2003).
14. B. O'Connor, K. H. An, Y. Zhao, K. P. Pipe, M. Shtein, "Fiber Shaped Organic Light Emitting Device", *Adv. Mat.* **19**, 3897 (2007).
15. B. O'Connor, K. P. Pipe, M. Shtein, "Fiber based organic photovoltaic devices", *Appl. Phys. Lett.* **92**, 193306 (2008).
16. M. Fokine, L. E. Nilsson, A. Claesson, D. Berlemont, L. Kjellberg, L. Krummenacher, and W. Margulis, "Integrated fiber Mach-Zehnder interferometer for electro-optic switching" *Opt. Lett.* **27**, 1643 (2002).
17. M. A. Schmidt, L. N. Prill Sempere, H. K. Tyagi, C. G. Poulton, and P. St. J. Russell, "Waveguiding and plasmon resonances in two-dimensional photonic lattices of gold and silver nanowires" *Phys. Rev. B*, **77**, 033417 (2008)
18. H. K. Tyagi, M. A. Schmidt, L. Prill Sempere and P. St. J. Russell, "Optical properties of photonic crystal fiber with integral micron-sized Ge wire", *Opt. Exp.* **16**, 17227 (2008).
19. M. Bayindir, F. Sorin, A. F. Abouraddy, J. Viens, S. D. Hart, J. D. Joannopoulos, Y. Fink, "Metal-Insulator-Semiconductor Optoelectronic Fibers", *Nature* **431**, 826 (2004).
20. A. F. Abouraddy, M. Bayindir, G. Benoit, S. D. Hart, K. Kuriki, N. Orf, O. Shapira, F. Sorin, B. Temelkuran, Y. Fink, "Towards multimaterial multifunctional fibres that see, hear, sense and communicate" *Nat. Mat.* **6**, 336 (2007).
21. M. Bayindir, A. F. Abouraddy, O. Shapira, J. Viens, D. Saygin-Hinczewski, F. Sorin, J. Arnold, J. D. Joannopoulos, Y. Fink, "Kilometer-long ordered nanophotonic devices by preform-to-fiber fabrication", *IEEE J. Sel. Top. Quantum Electron.*, **12** (6): 1202-1213 (2006)
22. F. Sorin, A. F. Abouraddy, N. Orf, O. Shapira, J. Viens, J. Arnold, J. D. Joannopoulos, Y. Fink, *Adv. Mater.* **19**, 3872-3877 (2007).
23. A. F. Abouraddy, O. Shapira, M. Bayindir, J. Arnold, F. Sorin, D. Saygin-Hinczewski, J. D. Joannopoulos, and Y. Fink, "Large-scale Optical-field measurements with geometric fiber constructs", *Nat. Mat.* **5** pp. 532-536 (2006).
24. F. Sorin, O. Shapira, Ayman F. Abouraddy, Matthew Spencer, Nicholas D. Orf, John D. Joannopoulos and Yoel Fink "Exploiting the collective effects of optoelectronic devices integrated in a single fiber" *NanoLetters*, **9** (7), 2630-2635 (2009).
25. M. Bayindir, O. Shapira, D. Saygin-Hinczewski, J. Viens, A. F. Abouraddy, J. D. Joannopoulos, Y. Fink, "Integrated fibers for self-monitored optical transport", *Nat. Mat.* **4**, 820 (2005).
26. M. Bayindir, A. F. Abouraddy, J. Arnold, J. D. Joannopoulos, Y. Fink, "Thermal-sensing mesoscopic fiber devices by composite-material processing" *Adv. Mater.* **18**, 845 (2006).
27. S. Egusa, Z. Wang, N. Chocat, Z. M. Ruff, A. M. Stolyarov, D. Shemuly, F. Sorin, P. T. Rakich, J. D. Joannopoulos and Y. Fink, "Multimaterial piezoelectric fibers", *Nat. Mat.* **9**, 643 (2010).
28. E. K. Sichel, J. I. Gittleman, P. Sheng, "Electrical properties of Carbon-polymer composite" *J. of Elec. Mat.* **11**, 699 (1982).
29. N. Orf, O. Shapira, F. Sorin, S. Danto, M. A. Baldo, J. D. Joannopoulos, Y. Fink, "Multimaterial Fiber Diodes via in situ Compound Synthesis" (manuscript under review).
30. E. Rosencher, B. Vinter, *Optoelectronics*, Cambridge University Press, New York (2002).

31. Sze, S. M. *Semiconductor Devices: Physics and Technology* 2nd edn (John Wiley, New York, (2001).
32. R. H. Kingston, *Detection of Optical and Infrared Radiation*, Springer-Verlag, Berlin, New York (1978).
33. Z. U. Borisova, *Glassy Semiconductors*, Plenum Press, New York,(1981).
34. S. Danto, F. Sorin, N.D. Orf, S.A. Speakman, Z. Wang, J. D. Joannopoulos and Y. Fink, "Fiber field-effect device via in-situ channel crystallization" *Adv. Mat.* (to be published).
35. D. S. Deng, N. D. Orf, A. F. Abouraddy, A. M. Stolyarov, J. D. Joannopoulos, H. A. Stone, and Y. Fink, "In-Fiber Semiconductor Filament Arrays", *Nano Lett.* **8**, 4265 (2008).